Nano Research

Open Access

Research Article

Facile method to synthesize conjugated poly(1,4-phenyldiimine) porphyrin cobalt with "electron pump" for enhancing bifunctional catalytic oxygen reaction performance

Yinggang Sun, Peng Sun, Jigang Wang, Yanqiong Zhuang, Likai Wang, Ang Li, and Zhongfang Li ✉

School of Chemistry and Chemical Engineering, Shandong University of Technology, Zibo 255049, China

Cite this article: *Nano Research*, **2025**, *18*, 94907789. https://doi.org/10.26599/NR.2025.94907789

ABSTRACT: To solve the slow dynamics of catalytic oxygen reaction energy devices, a facile method was developed for the synthesis of methylene alcohol terminated poly(1,4-phenyldiimine) porphyrin cobalt (M-PImPorCo), which was synthesized by $RuCl_3$ catalyzed redox reaction of meso-5,10,15,20-tetra(4-nitrophenyl) porphyrin cobalt (TNO_2PorCo) and 1,4-phenyldimethanol. M-PImPorCo is a fully conjugated covalent organic framework (COF) with high thermal and chemical stability. COFs with different edge groups were synthesized to compare the effect of different groups (–CH_2–OH and –NO_2) on catalytic bifunctional oxygen reaction activity. C=N as nitrogen-rich environment of M-PImPorCo leads to the protonation process of oxygen catalysis and reduces the energy barrier of adsorption in the oxygen intermediate. C=N and –CH_2–OH form an "electron pump" structure to deliver electrons to the Co–N_4 site in M-PImPorCo, and the π–π interaction between M-PImPorCo and three-dimensional graphene (3D-G) can further enrich the electron cloud density of Co–N_4 sites. M-PImPorCo/3D-G has remarkable oxygen catalytic performance, with a half-wave potential ($E_{1/2}$) of 0.91 V vs. reversible hydrogen electrode (RHE). M-PImPorCo/3D-G has low potential ($E_{j=10}$ is 1.49 V vs. RHE) at a current density of 10 mA·cm^{-2}. It exhibits a good bifunctional catalytic performance (potential difference (ΔE) = 0.58 V). The smaller charge–discharge band gap of zinc-air batteries (ZABs) and flexible ZABs (F-ZABs) equipped with M-PImPorCo/3D-G suggests the potential for catalytic oxygen reaction bifunctional applications. This work provides a new idea for the synthesis of Schiff-base porphyrin-based COF catalyst and its potential application to oxygen reaction catalytic energy storage devices.

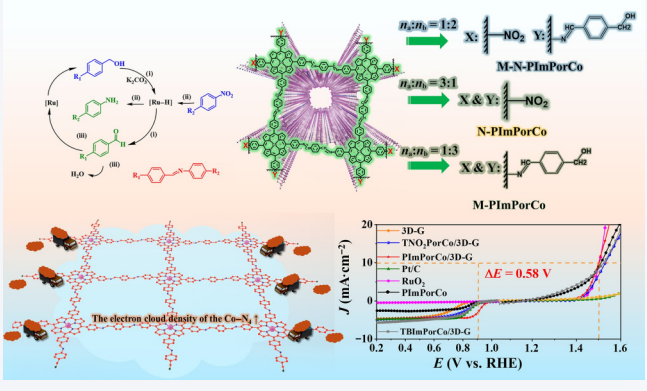

KEYWORDS: novel synthesis method, fully conjugated covalent organic frameworks, catalytic oxygen reduction reaction (ORR)/oxygen evolution reaction (OER) performance, methylene alcohol terminated poly(1,4-phenyldiimine) porphyrin cobalt (M-PImPorCo)/three-dimensional graphene (3D-G), electron pump

1 Introduction

With the exponential development of world economy, the demand of energy consumption has also been growing in the past decades [1]. It is essential to reduce our reliance on fossil fuels by developing sustainable and clean energy technologies, including fuel cells [2–5] and overall water splitting (OWS). The cathodes of fuel cells and anodes of OWS involve oxygen reduction reaction (ORR) [6–12] and oxygen evolution reaction (OER) [13, 14], respectively. The ORR entails the reduction of O_2 to H_2O in acidic media or OH^- in alkaline environments, proceeding primarily via a 4-electron pathway involving sequential proton-electron transfer steps and key intermediates, such as *O_2^-, *OOH, *O, and *OH, with O–O bond cleavage as the critical mechanistic step [9, 10]. In contrast, the OER, as the reverse process of ORR, involves the oxidation of H_2O (acidic) or OH^- (alkaline) to O_2 through a 4-electron transfer mechanism, characterized by the formation of surface-bound intermediates (*OH, *O, and *OOH) and the critical step of O–O bond formation [11]. Both reactions exhibit sluggish kinetics, with OER typically requiring higher overpotentials due to its more

Received: June 7, 2025; **Revised:** July 9, 2025
Accepted: July 10, 2025

✉Address correspondence to zhfli@sdut.edu.cn

complex mechanistic pathway, underscoring the necessity for rational catalyst design to stabilize key intermediates and lower activation barriers for efficient energy conversion. Slow kinetic process of the ORR and OER limits the energy conversion efficiency of the devices. Therefore, the efficient bifunctional catalyst is necessary for the oxygen conversion device. Rechargeable zinc-air batteries (ZABs) involve the ORR and the OER at their cathodes, which are typical devices for evaluating the bifunctional performance of oxygen reaction catalysts [15–18]. Development of cost-effective substitutes for Pt and Ru electrocatalysts for ORR and OER is crucial for fuel cells and OWS, respectively [19]. But their inherent scarcity and prohibitive costs severely hinder their application in sustainable energy systems. Recent research has focused on transition-metal-based catalysts, including transition-metal oxides (TMOs) [20, 21], transition-metal nitrides (TMNs) [17, 22], and transition-metal sulfides (TMSs) [23]. These materials leverage strategies to optimize the dispersion of active metal sites, enhance atomic utilization efficiency, and boost oxygen electrocatalytic activity through their electronic modulation [24].

Porphyrin is a natural oxygen catalyst that exists in nature. It is an important raw material for cytochrome P450 to catalyze the oxygen reduction process. Metalloporphyrin (PorM) is also considered a promising oxygen reaction catalyst. However, the catalytic ORR performance of PorM is still unsatisfactory in comparison with the benchmark platinum-carbon (Pt/C), which might be limited by the undesired thermal stability toward heat treatment (HT) [25]. PorM is pyrolyzed to obtain metal-nitrogen-carbon (M-N-C) atom clusters during HT process [26], and the clusters have low metal atom utilization, unclear active site, and poor stability [27–29]. Therefore, it is necessary to link metal porphyrins to form covalent organic framework (COF) structure [30, 31].

There are many applications of PorM-COF to electrocatalysis, which can be divided into general COF and fully conjugated COF (FCPorM-COF): (1) Non-fully conjugated COFs do not have fully conjugated structures, so their thermal and chemical stability is poor, like monocyclic porphyrins. In previously reported work [32, 33], COF often requires pyrolysis to obtain metal-nitrogen-carbon atomic clusters, which greatly reduces the atomic utilization and oxygen reaction catalytic performance. In addition, general COF without HT showed poor oxygen reaction catalytic performance. (2) The FCPorM-COF has larger conjugated π bonds and higher delocalization energy, which gives FCPorM-COF higher thermal and chemical stability. FCPorM-COF has a smaller highest occupied molecular orbital–lowest unoccupied molecular orbital (HOMO–LUMO) energy gap than monocyclic porphyrin [34], which enables FCPorM-COF to exhibit an easier electron-accepting ability and electron-donating (releasing) ability than monocyclic porphyrins [35, 36]. For example, the self-polymerized metal porphyrin framework has a fully conjugated structure [37, 38]; its lower HOMO–LUMO energy gap enhances its electron gain and loss ability. High delocalization energy enhances its thermal stability (it is not decomposed at 600 °C). Fully conjugated COF linked by azo groups has a good thermal stability, and the nitrogen-rich environment is more favorable to catalytic oxygen reaction process [39]. The linking groups, as electron-donating groups, can enrich the electron cloud density at the Co–N_4 sites, thereby enhancing the catalytic performance in oxygen reactions. The fully conjugated poly(benzimidazole porphyrin-cobalt) (PBIPorCo) obtained by linking with benzimidazole groups exhibits excellent bifunctional performance in catalyzing oxygen reactions [18]. FCPorM-COF with imine groups is a typical Schiff base polymer, which has not only high thermal stability but also good electrocatalytic activity. C=N as nitrogen-rich environment enhances oxygen reaction catalytic performance of FCPorM-COF [40–42]. For example, COF-366 with C=N groups is defined as FCPorM-COF—a typical fully conjugated COF linked by imine groups. It exhibits good thermal stability and has been applied in the catalytic CO_2 reduction reaction (CO_2RR) [43]. Schiff base FCPorM-COF is usually prepared by meso-5,10,15,20-tetra(4-amino phenyl porphyrin) and meso-5,10,15,20-tetra(4-aldehyde phenyl porphyrin) [2, 44]. However, this reaction has following problems: (1) These two raw materials are expensive and difficult to obtain and store. (2) Schiff base FCPorM-COF has fixed structure with uncontrollable COF structure and edge groups. Therefore, it is of great significance to find a facile method to synthesize the Schiff base FCPorM-COF. Previous reports have proposed that $RuCl_3$ catalyzes redox reactions between $-NO_2$ and $-CH_2-OH$ functional groups in small molecular compounds to synthesize Schiff base group structures [45]. Can this method be used to prepare the macromolecular compound FCPorM-COF?

This method can not only conveniently prepare the fully conjugated imine group FCPorM-COF, but also has the following advantages: (1) The raw materials are readily available, low-cost, and easy to store. (2) The structure of FCPorM-COF can be regulated, and the edge-modifying groups can be adjusted. The prepared compounds have the following advantages: (1) The delocalization energy of FCPorM-COF will increase, and its conjugated system will be extended, which could enhance the thermal and chemical stability of FCPorM-COF; (2) FCPorM-COF has a smaller HOMO–LUMO energy gap than monocyclic porphyrin, which enhances its electron gain and loss in the catalytic redox reaction; (3) C=N as nitrogen-rich environment in FCPorM-COF promotes the protonation process of intermediates during oxygen reaction catalysis; and (4) The edges of FCPorM-COF could all be modified by strong electron donor groups ($-CH_2-OH$), which can increase electron cloud density of the catalytic center M–N_4.

Complex topology often limits conductivity and active centers distribution of FCPorM-COF. Anchoring FCPorM-COF on the surface of electronic conductor after solvation and heat treatment is a strategy to improve the dispersion of active center and conductivity. Three-dimensional graphene (3D-G) is a kind of excellent electronic conductor with the characteristic π bonds of graphene. Its porous structure can not only play a supporting role, but also strengthen mass transfer in catalytic process. Large π bonds of graphene could form π–π interactions with FCPorM-COF [20], which promotes the catalytic oxygen reaction bifunctional performance of the FCPorM-COF/3D-G. Therefore, FCPorM-COF anchored on 3D-G surface has the following advantages: (1) There are π–π interactions between FCPorM-COF and 3D-G, which can synergistically promote catalytic oxygen reaction performance and (2) C=N groups and $-CH_2-OH$, as strong electron absorbing group and electron donating groups, respectively, transfer electrons and promote electron cloud density of Co–N_4 due to the formation of a "donor–π–acceptor (D–π–A)" structure [39].

Herein, a fully conjugated two-dimensional (2D) methylene alcohol terminated poly(1,4-phenyldiimine) porphyrin cobalt (M-PImPorCo) was synthesized by $RuCl_3$ catalyzed redox reaction of meso-5,10,15,20-tetra(4-nitrophenyl) porphyrin cobalt

(TNO_2PorCo) and 1,4-phenyldimethanol. The different groups terminated poly(1,4-phenyldiimine) porphyrin cobalt were prepared by adjusting the ratio of reactants to compare effect of different edge groups on the oxygen reaction catalytic performance of FCPorM-COF. Meso-5,10,15,20-tetra(4-methoxypheny-liminophenyl) porphyrin cobalt (TmPorCo) was prepared to compare the effect of conjugation on the structure and oxygen reaction catalytic performance of FCPorM-COF. M-PImPorCo was obtained by adjusting the reactant ratio, and its structure was characterized by ultraviolet–visible (UV–Vis) spectroscopy, Fourier transform infrared (FT-IR), ^{13}C nuclear magnetic resonance (^{13}C NMR) spectra, Brunauer–Emmett–Teller (BET), the high-resolution transmission electron microscope (HRTEM), and powder X-ray diffraction (PXRD). Material studios (MS) theoretical simulations were used to determine the pore structure and the topological structure configurations of the tetra-connected sql network. The elemental composition and valence states of COF were characterized by X-ray photoelectron spectroscopy (XPS). Thermogravimetric (TG) was used to determine the thermal stability of COF. M-PImPorCo was loaded onto 3D-G and HT at 600 °C to form M-PImPorCo/3D-G. UV–Vis diffuse reflection spectra (UV–Vis–DRS), Raman spectra, PXRD, scanning electron microscope (SEM), TEM, and XPS were used to study the internal interaction of M-PImPorCo/3D-G. The performance of catalytic ORR and OER was studied to evaluate the catalytic oxygen reaction bifunctional performance of M-PImPorCo/3D-G. To further investigate the oxygen reaction catalysis process of COF, density functional theory (DFT) calculations were performed based on first-principles methods. ZABs were assembled with M-PImPorCo/3D-G catalyst as cathode to evaluate the catalytic oxygen reaction bifunctional performance.

2 Experimental

2.1 Materials

4-Nitrobenzaldehyde, cobalt(II) acetate tetrahydrate, 1,4-benzenedimethanol, N,N-dimethylformamide (DMF), N,N-dimethylacetamide (DMAc), acetic acid, propionic acid, nitrobenzene, methanol, and potassium hydroxide (KOH) were purchased from Sinopharm Chemical Reagent Co., Ltd. Coal tar pitch (CTP) was purchased from a local chemical factory. $CaCO_3$ (20 nm) was purchased from Taiji Ring Nano Co., Ltd. Nafion was purchased from DuPont Company. Pt/C catalyst (20.0%) and RuO_2 were purchased from E-TEK Co., Ltd. and Anhui Senrise Technology Co., Ltd., respectively. Carbon cloth was purchased from CeTech Co., Ltd. Pyrrole was purchased from Energy Chemical Co., Ltd. All chemicals were analytical reagent (AR) grade, and no further purification was required for use. The synthesis of TNO_2PorCo is in Section S1.1 in the Electronic Supplementary Material (ESM).

2.2 Synthesis of poly(1,4-phenyldiimine) porphyrin cobalt with different terminal groups

TNO_2PorCo (0.425 g, 0.500 mmol), 1,4-phenyldimethanol (0.2075 g, 1.5 mmol), K_2CO_3 0.500 g, 3.6 mmol), and $RuCl_3{\cdot}3H_2O$ (0.025 g, 0.110 mmol) were dissolved in DMF (150 mL), before being subjected to $RuCl_3$ catalyzed polymerization for 24 h at 135 °C. The reaction mechanism is shown in Fig. S1 in the ESM. During the reaction process, a drying tube filled with anhydrous $CaCl_2$ was added to remove the water vapor generated in the reaction. After the reaction was completed, the reactants were steamed to paste, immersed in a 500 mL dilute acetic acid solution (to inhibit the hydrolysis of Ru^{3+}), pumped, and filtered to obtain crude products. Finally, the purple-black solid was obtained by recrystallization three times with DMF. The product, synthesized from TNO_2PorCo and 1,4-phenyldimethanol in a molar ratio of 1:3, was named M-PImPorCo (0.424 g, yield ~ 70.0%).

The preparation method for other edge-modified COFs was identical, with only raw material ratios adjusted: The product synthesized at a TNO_2PorCo to 1,4-phenyldimethanol molar ratio of 1:2 was named methylene alcohol and nitro-terminated poly(1,4-phenyldiimine) porphyrin cobalt (M-N-PImPorCo, with a methylene alcohol:nitro termination ratio of 1:1) (Fig. S4 in the ESM), while the material synthesized at a 3:1 ratio was named nitro-terminated poly(1,4-phenyldiimine) porphyrin cobalt (N-PImPorCo) (Fig. S5 in the ESM).

To investigate effects of electron-donating groups and the conjugation effects of fully conjugated M-PImPorCo with electron-donating groups, TmPorCo was designed and synthesized. The synthesis method was the same as the previous one, but to obtain a monocyclic porphyrin structure, 1,4-diphenylcarbinol was replaced with 4-methoxybenzyl alcohol, and molar ratio of TNO_2PorCo to 4-methoxybenzyl alcohol was controlled at 1:3.

2.3 Preparation of M-PImPorCo/3D-G

0.100 g of M-PImPorCo was dissolved in 90 mL of DMAc and the solution was heated to 155 °C. 0.100 g of 3D-G was dispersed in 90 mL DMAc, added into the above mixture solution, and refluxed for 24 h. DMAc was removed by distillation under reduced pressure to give a black paste precursor. The black precursor was dried under vacuum at 60 °C for 12 h to obtain a black solid. The solid powder was ground and heat-treated at 600 °C under N_2 for 2 h. The product was named M-PImPorCo/3D-G.

The series of samples was prepared according to the mass ratio of 3D-G and M-PImPorCo (1:2, 1:1, and 2:1), and then heat-treated at 600 °C, and the samples obtained were named M-PImPorCo/3D-G-1-2, M-PImPorCo/3D-G, and M-PImPorCo/3D-G-2-1, respectively.

M-PImPorCo/3D-G prepared at 500, 600, and 700 °C were named M-PImPorCo/3D-G-500, M-PImPorCo/3D-G, and M-PImPorCo/3D-G-700, respectively.

TNO_2PorCo/3D-G, TmPorCo/3D-G, N-PImPorCo/3D-G, and M-N-PImPorCo/3D-G were prepared via the same method, with a mass ratio of 1:1, and under HT at 600 °C

3 Results and discussion

3.1 Synthesis and structural characterization of M-PImPorCo

M-PImPorCo was synthesized by TNO_2PorCo and 1,4-phenyldimethanol, catalyzed by $RuCl_3$ (Scheme 1(a)), and the reaction mechanism is shown in Fig. S1 in the ESM. Figure S2 in the ESM shows the preparation of different edge group terminated COFs by adjusting the ratio of TNO_2PorCo to 1,4-phenyldimethanol. M-PImPorCo is a fully conjugated COF with strong electron-donating groups ($-CH_2-OH$) at the edges (Fig. S3 in the ESM). N-PImPorCo is a fully conjugated COF with a strong electron-withdrawing group ($-NO_2$) at the edge (Fig. S5 in the ESM), and M-N-PImPorCo is a COF with both groups at the edge

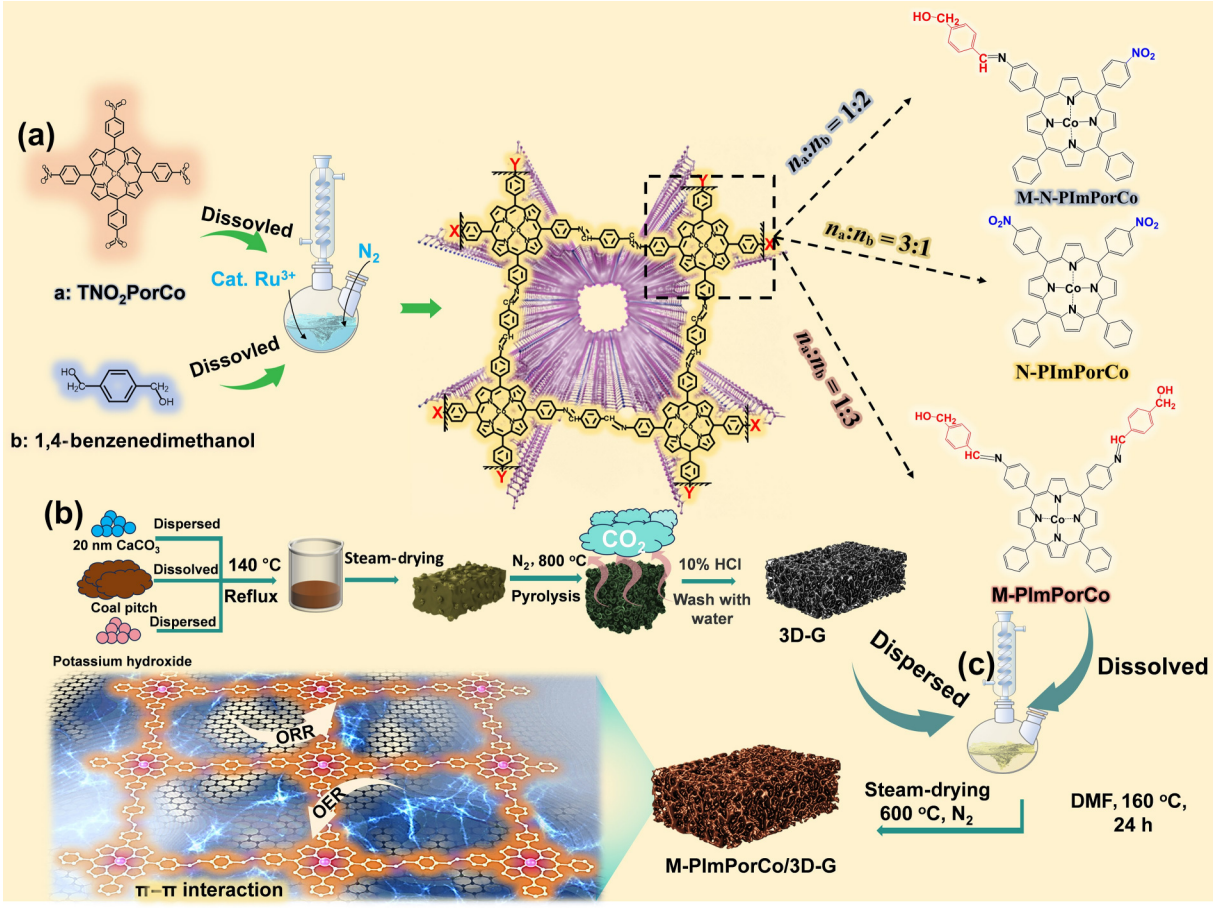

Scheme 1 Preparation process of M-PImPorCo and M-PImPorCo/3D-G.

(–CH_2–OH and –NO_2 ratio is 1:1) (Fig. S4 in the ESM). To compare the effect of conjugation on catalytic performance, monocyclic porphyrin complexes with electron-donating groups (TmPorCo) were synthesized in the same way as M-PImPorCo (Fig. S6 in the ESM).

UV–Vis spectra were used to characterize TNO_2PorCo and M-PImPorCo, which both have two absorption peaks (Fig. 1(a)). Absorption peaks belong to the Soret band (440.4 nm in TNO_2PorCo and 449.4 nm in M-PImPorCo) and the quadrupole band (Q band) (557.6 nm in TNO_2PorCo and 567.6 nm in M-PImPorCo) caused by the π to π* transition in conjugated system. Due to the conjugation effect, the delocalization energy of the porphyrin plane increases, and Soret band and Q band of M-PImPorCo red shift by 11 and 8 nm in comparison with TNO_2PorCo, respectively. TmPorCo has Soret and Q band absorption peaks (Fig. S7 in the ESM). Compared with TNO_2PorCo, the Soret absorption peak and Q band red shift by 2 and 3 nm, respectively, which proves that the CH_3–O– edge is linked. Chemical compositions of M-PImPorCo were verified through FT-IR spectra. As displayed in Fig. 1(b), successful formation of the C=N bonds within the structures is confirmed by the presence of a characteristic peak at 1680 cm^{-1} in M-PImPorCo, accompanied by a reduction in the intensity of –C–O at 1160 cm^{-1} stretching bands. Moreover, the distinct peak at approximately 846 cm^{-1} is attributed to the Co–N tensile vibration [37]. In addition, there is a relatively weak peak at 964 cm^{-1}, which is caused by bending vibration of the porphyrin rings [46]. The vibrational strength of –NO_2 (1540 cm^{-1}) in M-PImPorCo is not observed, which proves that –NO_2 was consumed to form C=N during polymerization. Apparent presence of –CH_2– (2980 cm^{-1}) and –OH (3600 cm^{-1}) indicates the occurrence of polymerization. Chemical structure of M-PImPorCo was further confirmed by ^{13}C NMR, as shown in Fig. 1(c), ^{13}C NMR spectrum of M-PImPorCo (400 MHz, deuterated dimethyl sulfoxide (DMSO-d_6), ppm): C peak at chemical shift (δ) = 160 corresponds to the C=N, and δ = 64.7 corresponds to the –CH_2–. The other peaks: δ = 115.4, 120.2, 121.2, 122.2, 124.9, 127.7, 129.4, 129.5, 130.5, 135.3, 135.8, 137.0, 138.6, 140.8, 146.6, 151.2, belong to b'–q' type C peaks, respectively [44, 47]. The O–CH_3 and C=N at 55.8 and 160.0 characteristic peaks in ^{13}C NMR spectrum also verify the precise structure of TmPorCo (Fig. S8 in the ESM). The N_2 sorption and BET method were employed to characterize the pore structure of M-PImPorCo, and characteristic pore size of 2.3 nm is found in Fig. 1(d), which corresponds to the theoretical simulation of M-PImPorCo (A–B stacking and A–A stacking) (Fig. S9 in the ESM). The isothermal adsorption and desorption show Type III curves, and the BET specific surface area is 85.4 $m^2 \cdot g^{-1}$, which is primarily attributed to its topological stacking and the spatial steric effects of its edge groups. Structurally, M-PImPorCo adopts an eclipsed A–A stacking topology in a *Pm* space group, leading to dense layer-by-layer arrangements that minimize interlayer spacing and restrict the formation of large accessible pores. This compact stacking significantly reduces the overall pore volume and surface area [48]. Additionally, the edge groups (–CH_2–OH) introduce spatial steric effects that may further influence pore formation and distribution [49]. The combination of tight topological stacking and edge group steric effects results in a characteristic pore size of 2.3 nm, primarily composed of mesopores, which inherently contributes to the lower

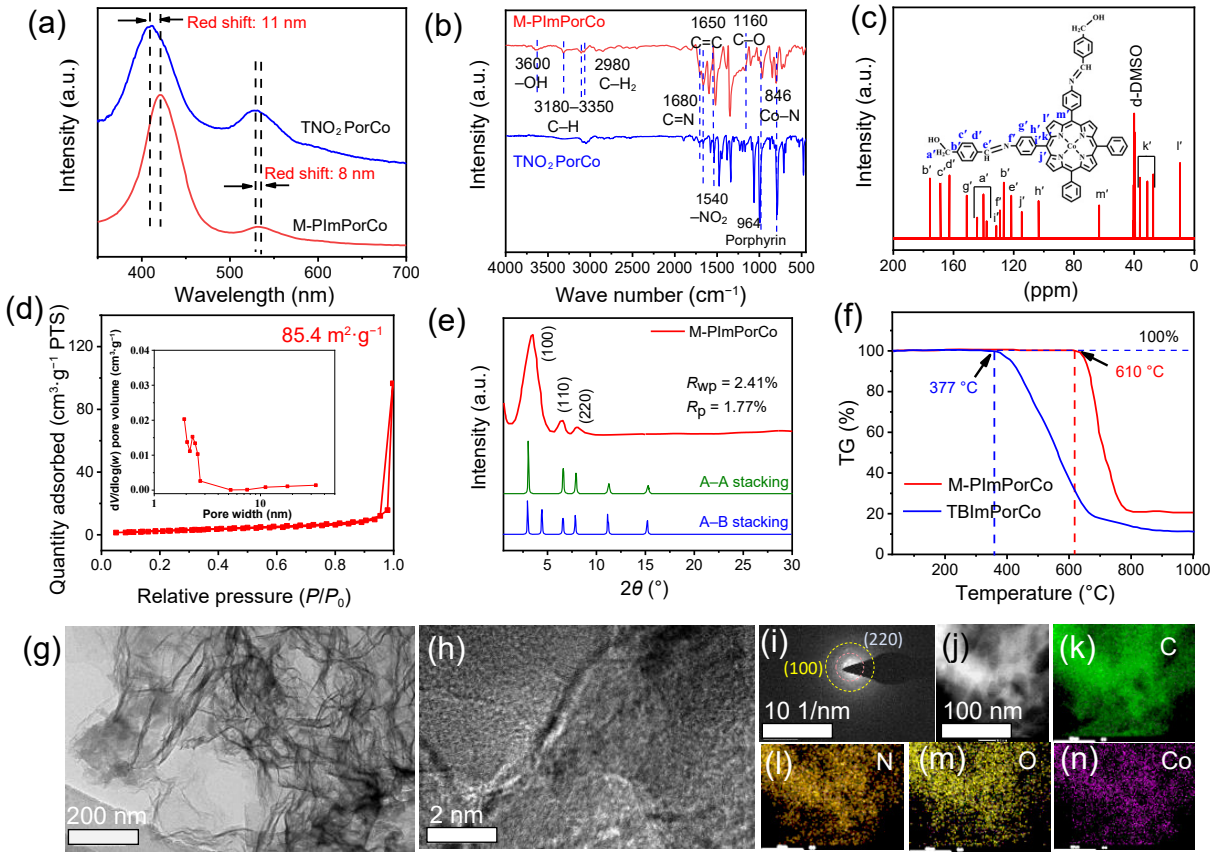

Figure 1 The characterization of samples: (a) UV–Vis and (b) FT-IR spetra of TNO_2PorCo and M-PImPorCo; (c) ^{13}C NMR spectrum of M-PImPorCo (solvent as DMSO-d_6); (d) nitrogen adsorption–desorption isotherms and pore-size distribution plots for the sample; (e) PXRD patterns, (f) TG curves, and (g) TEM and (h) HRTEM images of M-PImPorCo; (i) SAED pattern and (j) HAADF-STEM image of M-PImPorCo; and ((k)–(n)) mappings of (k) C, (l) N, (m) O, and (n) Co.

BET surface area compared to materials with more open or hierarchical pore structures.

Figure 1(e) shows that Pawley refinements were applied to investigate the theoretical structures with the self-consistent charge density functional tight binding (DFTB) method. M-PImPorCo adopts an eclipsed stacking in a *Pm* space group with refined cell parameters of a = 48 Å, b = 48 Å, and c = 3 Å. Experimental results were simulated with weighted profile residual factor (R_{wp}) of 2.41% and profile residual factor (R_p) of 1.77%, respectively. Both eclipsed (A–A) and staggered (A–B) stacking structures were simulated for the COF, and the A–A simulated PXRD pattern of the eclipsed structures has a much better match with the experimental results. TG was used to test the thermal stability of M-PImPorCo (Fig. 1(f)). The thermal stability of M-PImPorCo was tested in the N_2 atmosphere at 30–1000 °C. The weight loss begins at 610 °C, and it can be maintained within 600 °C without weight loss. Therefore, M-PImPorCo is not decomposed during HT at 600 °C. TmPorCo decomposes at 370 °C, which proves that M-PImPorCo conjugated structures can improve thermal stability. To further study the porous structure of M-PImPorCo, SEM was used to exhibit the morphology of M-PImPorCo. As depicted in Fig. S10 in the ESM, the as-prepared M-PImPorCo exhibited a highly homogeneous layer stacking topology. According to energy dispersive X-ray (EDX) plane scans, the atomic ratios of each element are close to the structure of M-PImPorCo (Fig. S11 in the ESM). As shown in Fig. 1(g), TEM shows that M-PImPorCo has a stacked topological structure. In HRTEM (Fig. 1(h)), M-PImPorCo has clear lattice fringes corresponding to the (220) crystal plane in XRD patterns, which can be found in the fast FT (FFT) (Fig. 1(i)). High-angle annular dark-field (HAADF) (Fig. 1(j)) represents the uniform dispersion of different atoms. Element mapping and scanning TEM (STEM) showed that 4 different elements (C, N, O, and Co) were uniformly dispersed in M-PImPorCo (Figs. 1(k)–1(n)).

3.2 Preparation and structural characterization of M-PImPorCo/3D-G

To improve the conductivity and Co–N_4 site dispersion effect of M-PImPorCo, M-PImPorCo/3D-G was prepared by enhanced impregnation (Scheme 1(c)). UV–Vis diffuse reflectance absorption spectra of the M-PImPorCo and M-PImPorCo/3D-G are shown in Fig. 2(a). Compared with M-PImPorCo, the Soret band and the Q band of M-PImPorCo/3D-G red shift by 11 and 8 nm, respectively. It indicates the π–π interaction occurring between M-PImPorCo and 3D-G [34]. Raman spectra data of M-PImPorCo/3D-G and 3D-G (Fig. 2(b)) show that the D and G peaks represent the extent of defect and graphitization in sp^2 carbon, respectively [17]. I_D/I_G (I_D represents intensity of D peak and I_G represents intensity of G peak) values for M-PImPorCo/3D-G and 3D-G are 0.97 and 0.90, respectively, which proves that M-PImPorCo/3D-G has a more defect-abundant structure than 3D-G, and exposes more active sites [50]. Meanwhile, no absorption peaks of M-PImPorCo stacking are detected on the catalyst [51]. Notably, the G peak in M-PImPorCo/3D-G experiences a significant red shift (27 cm^{-1}) compared to 3D-G due to π–π interaction occurring between M-

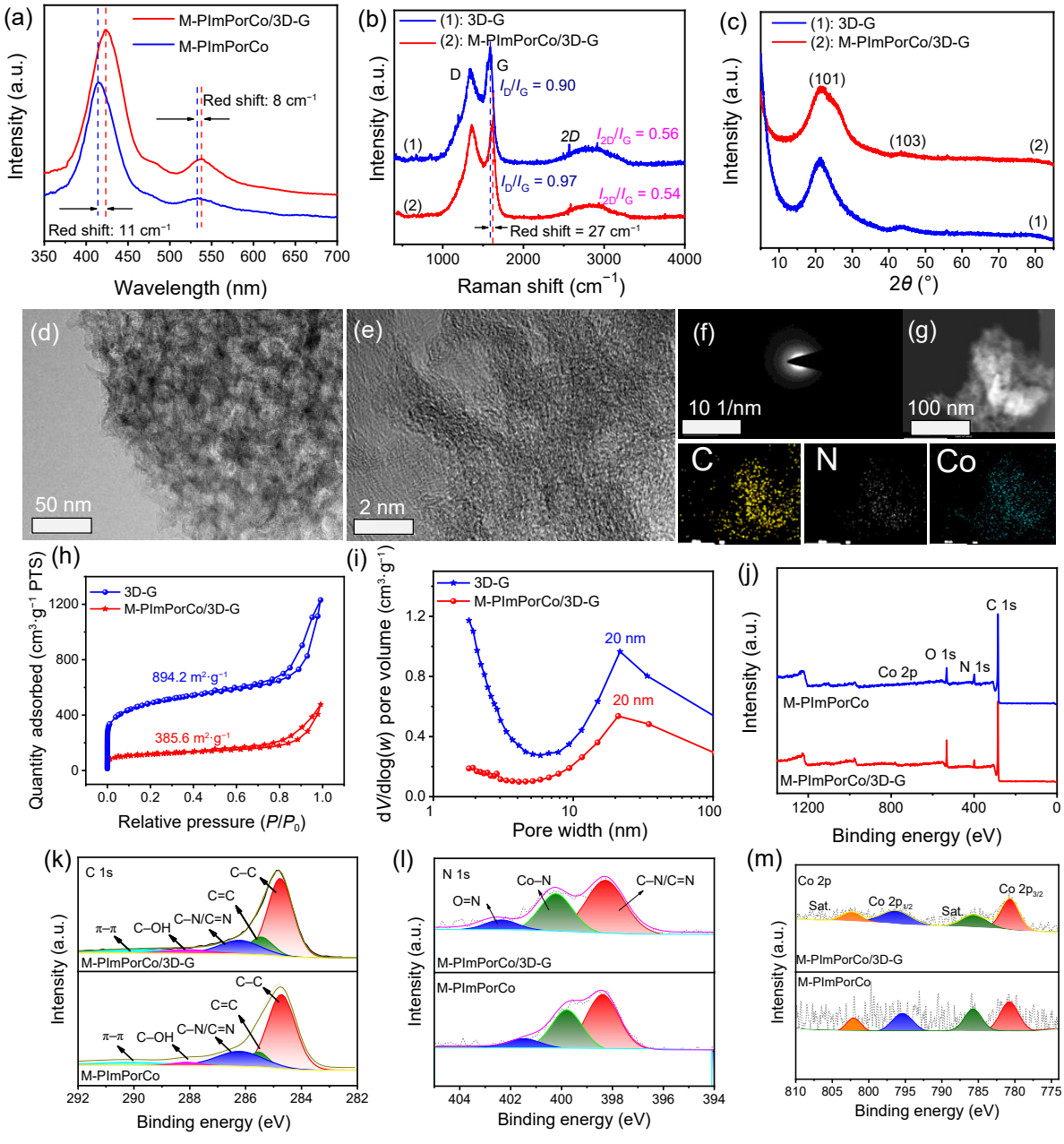

Figure 2 The characterization of M-PImPorCo/3D-G and M-PImPorCo: (a) UV–Vis diffuses reflectance absorption spectra; (b) Raman spectra; (c) XRD patterns of M-PImPorCo/3D-G and 3D-G; ((d) and (e)) TEM and HRTEM images of M-PImPorCo/3D-G; (f) SAED pattern; (g) HAADF-STEM image and mappings of C, N, and Co; (h) BET surfaces and (i) pore size distribution; and (j) XPS full spectra. ((k)–(m)) The high-resolution XPS spectra of M-PImPorCo and M-PImPorCo/3D-G: (k) C 1s, (l) N 1s, and (m) Co 2p.

PImPorCo and 3D-G (Fig. S12 in the ESM) [37]. An obvious 2D peak is observed at 2800 cm^{-1}. The calculated I_{2D}/I_G (I_{2D} represents the intensity of 2D peak) ratios of M-PImPorCo and 3D-G are 0.56 and 0.54, respectively, which indicates that it is multilayer graphene with 3–7 layers. This proves that M-PImPorCo is close to single layer laid on the 3D-G surface [52]. In the PXRD patterns (Fig. 2(c)), M-PImPorCo/3D-G shows only the characteristic diffuse reflection peaks of graphene and no other obvious peaks when compared with 3D-G [53]. The results show that: (1) M-PImPorCo is not decomposed in HT process. (2) M-PImPorCo does not stack, and it is laid on 3D-G surface. SEM shows that M-PImPorCo/3D-G retains the multi-channel structure of 3D-G (Fig. S13 in the ESM), and its abundant multistage channels can be observed. TEM (Fig. 2(d)) demonstrates that M-PImPorCo/3D-G is a foam-like porous graphene structure. In HRTEM (Fig. 2(e)) and selected area electron diffraction (SAED) (Fig. 2(f)), M-PImPorCo/3D-G only shows carbon layer fringes without other lattices, indicating that there are no oxides or M-N-C clusters of Co-N-C, and it is not decomposed during in HT process. M-PImPorCo is not stacked and is not decomposed, and is laid on the 3D-G surface. HAADF-STEM images (Fig. 2(g)) clearly reveal the uniform distribution of C, N, and Co on the 3D-G surface. The N_2 sorption isotherms and pore size distribution are shown in Figs. 2(h) and 2(i). M-PImPorCo/3D-G exhibits surface area of 385.6 m^2·g^{-1}, and the specific surface area of M-PImPorCo/3D-G is smaller than that of 3D-G (894.2 m^2·g^{-1}), which is explained by the

fact that M-PImPorCo is anchored to the 3D-G surface. Mesoporous and microporous structures were abundant in 3D-G due to CO_2 decomposition by $CaCO_3$ during the pyrolysis process, resulting in multi-level pore structure formation. Additionally, there is a distinct characteristic peak at around 20 nm attributed to mesopores generated by template $CaCO_3$ (Fig. 2(i)). M-PImPorCo/3D-G retains the pore size distribution characteristic of 3D-G, while the number of micropores and mesopores within the 1–3 nm range is reduced. Both the specific surface area and pore width of M-PImPorCo/3D-G decrease owing to the deposition of M-PImPorCo on the surface of 3D-G. M-PImPorCo/3D-G has multi-level channels, which is beneficial to enhance mass transfer during catalytic oxygen reaction process.

Surface chemistry composition and valence state of M-PImPorCo and M-PImPorCo/3D-G were detected by XPS, which reveals the presence of C, N, and Co elements (Fig. 2(j) and Table S1 in the ESM). It shows that the composition and proportion of each element are similar between M-PImPorCo and M-PImPorCo/3D-G. The ratio of Co element in M-PImPorCo and M-PImPorCo/3D-G is close to 2:1, which is consistent with the ratio of M-PImPorCo and 3D-G. The deconvolution of C 1s signals reveals peaks at 284.5, 285.4, 286.1, 288.1, 290.6 eV, corresponding to C–C, C=C, C–N/C=N, –C–OH, and π–π [29, 54, 55], respectively (Fig. 2(k)). Similarly, the high-resolution N 1s spectra consist of three peaks at 398.7, 399.8, and 402.1 eV for C–N/C=N, Co–N, and O=N, respectively [56, 57] (Fig. 2(l)). In addition, two sets of peaks at 780.4 and 796.2 eV in the Co 2p XPS spectra indicate that cobalt sites in M-PImPorCo and M-PImPorCo/3D-G are in an intermediate oxidation state [18, 58] (Fig. 2(m)). Compared with M-PImPorCo, XPS spectra of M-PImPorCo/3D-G show that chemical states of each element have not changed after HT, which proves that M-PImPorCo remains its structure during the HT process. Combined with TG, XPS, HRTEM, PXRD, and Raman spectra, the conclusions are as following: (1) M-PImPorCo is not decomposed after the HT (at 600 °C); (2) M-PImPorCo does not stack and lies flat on the surface of 3D-G; (3) M-PImPorCo has π–π interaction with 3D-G; and (4) M-PImPorCo/3D-G is a single-atom catalyst (SAC), and Co–N_4 is the activity site. Inductively coupled plasma-mass spectrometry (ICP-MS) is shown in Table S3 in the ESM. The total Co contents in M-PImPorCo and M-PImPorCo/3D-G electrocatalyst are about 3.52 wt.% and 1.50 wt.%, respectively.

3.3 Oxygen reduction reaction performance evaluation

ORR performance of as-prepared catalysts was evaluated by cyclic voltammetry (CV) measurements. As shown in Fig. S14 in the ESM, the voltametric profiles of all samples exhibit quasi-rectangular double-layer capacity current in a N_2 saturated 0.1 M KOH solution; no obvious redox peak is found. On the contrary, the well-defined cathodic peaks are displayed in O_2-saturated 0.1 M KOH, confirming effective reduction of oxygen. Linear sweep voltammetry (LSV) curves (Fig. S15 in the ESM) were measured in O_2-saturated 0.1 M KOH. It is observed that M-PImPorCo/3D-G exhibits the best performance among the series of all samples due to the optimization of catalyst preparation process. In a series of samples prepared, M-PImPorCo/3D-G, with an optimal activation temperature of 600 °C and an optimal ratio of 1:1, is the best performing catalyst. As depicted in Fig. 3(a), half-wave potentials ($E_{1/2}$) of M-PImPorCo/3D-G, M-N-PImPorCo/3D-G, N-PImPorCo/3D-G, TmPorCo/3D-G, and Pt/C are measured as 0.91, 0.89, 0.88, 0.81, and 0.85 V vs. reversible hydrogen electrode (RHE), respectively. The activity order of samples is M-PImPorCo/3D-G > M-N-PImPorCo/3D-G > N-PImPorCo/3D-G. The results show that electron donor groups can improve the catalytic activity. As shown in Fig. S16(a) in the ESM, the half-wave potentials of TNO_2PorCo/3D-G, M-PImPorCo, and 3D-G are measured as 0.83, 0.81, and 0.78 V vs. RHE, respectively. It proves that catalytic ORR performance is improved after the M-PImPorCo anchoring of 3D-G. The performance of M-PImPorCo/3D-G is better than that of TNO_2PorCo/3D-G and TmPorCo/3D-G, which is the effect of conjugation on catalytic ORR performance. M-PImPorCo/3D-G exhibits an $E_{1/2}$ 60 mV higher than Pt/C. To investigate the reaction kinetics of electrocatalysts, the Tafel plots were analyzed and the results are displayed in Fig. 3(b) and Fig. S16(b) in the ESM, where the Tafel slope is about 58, 60, 68, 77, 78, 76, 125, and 65 mV·dec^{-1} for M-PImPorCo/3D-G, M-N-PImPorCo/3D-G, N-PImPorCo/3D-G, TmPorCo/3D-G, TNO_2PorCo/3D-G, M-PImPorCo/3D-G, and 20 wt.% Pt/C, respectively. The lowest Tafel slope indicates that M-PImPorCo/3D-G has the fastest ORR kinetics, which makes it an attractive option for ORR applications. Rotating ring-disk electrode (RRDE) technique was carried out to determine the production of hydrogen peroxide (Fig. 3(c) and Fig. S17 in the ESM). M-PImPorCo/3D-G catalyst exhibits a H_2O_2 yield below 16.6% within 0.2–0.8 V potential range, with corresponding electron transfer number (n) calculated as 3.85–3.96. This further confirms that ORR process on M-PImPorCo/3D-G proceeds via 4-electron reaction pathway. To explore the ORR mechanism, LSV curves of M-PImPorCo/3D-G with different rotation speeds were analyzed and the results are shown in Fig. S18 in the ESM. The corresponding Koutecký–Levich (K–L) plots exhibited good linearity with a consistent slope at different potentials, implying that the ORR process followed first-order reaction kinetics with respect to the dissolved O_2 concentration. Electron transfer number consistent with K–L equation could be observed for other samples in Fig. S19 in the ESM. Figure 3(d) shows $E_{1/2}$ of M-PImPorCo/3D-G decreased from 0.91 to 0.82 V vs. RHE after poisoning experiments. Furthermore, it was observed that in O_2-saturation conditions, the oxygen reduction activity of M-PImPorCo could be fully recovered. $[SCN]^-$ can form complexes with Co^{2+}, providing evidence for the presence of the Co–N_4 site through poisoning experiments. Poisoning experiment results confirm that Co–N_x sites in M-PImPorCo/3D-G serve as active sites for oxygen catalytic reactions [59].

After continuous chronoamperometric measurement for 50,000 s (current–time (i–t)) (Fig. 3(e)), the initial current of M-PImPorCo/3D-G, TNO_2PorCo/3D-G, and Pt/C catalysts lost 10%, 14%, and 33%, respectively. It is well known that the stability is another critical descriptor to evaluate the performance of electrocatalysts. Catalytic cycling stability was evaluated via accelerated durability testing (ADT). As displayed in Fig. S20 in the ESM and Fig. 3(f), the $E_{1/2}$ of TNO_2PorCo/3D-G and Pt/C shows an obvious negative shift of 15 and 29 mV after 5000 cycles, respectively, while only an 11 mV negative shift for M-PImPorCo/3D-G reveals satisfactory stability. It increases the delocalization energy within PorM and improves its chemical stability, which enhances the electrochemical stability of M-PImPorCo/3D-G. The catalytic ORR performances of M-PImPorCo, M-PImPorCo/3D-G, and Pt/C in 0.5 M H_2SO_4 electrolyte are shown in Fig. S21 in the ESM. The $E_{1/2}$ of M-PImPorCo/3D-G, M-PImPorCo, and Pt/C are 0.80, 0.77, and 0.83 V, respectively. It is implied that M-PImPorCo/3D-G has good performance in proton exchange membrane fuel cell (PEMFC).

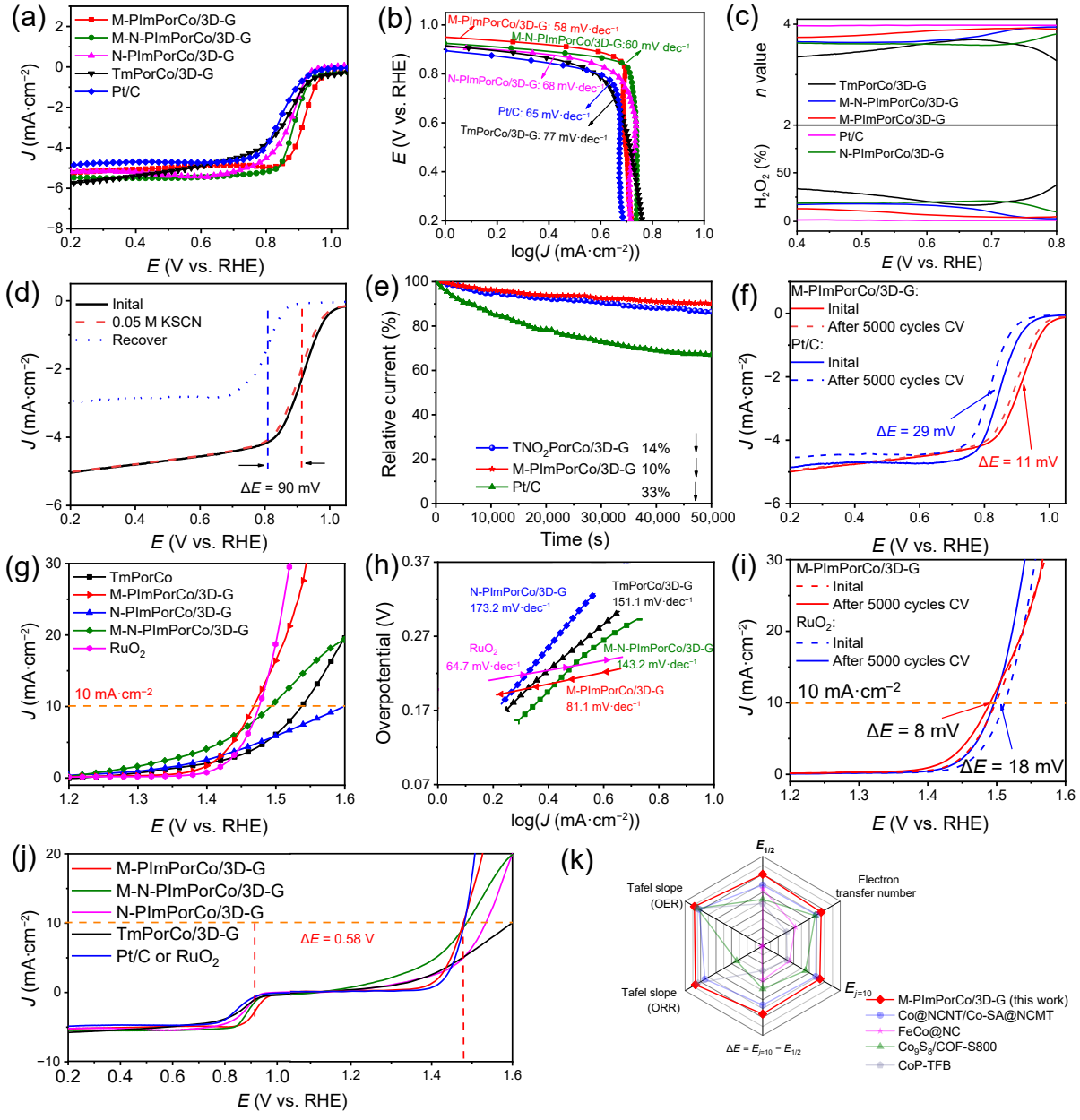

Figure 3 The ORR and OER test performance evaluation. The ORR test in 0.1 mol·L^{-1} KOH: (a) LSV curves of M-PImPorCo/3D-G, N-PImPorCo/3D-G, and M-N-PImPorCo/3D-G, TmPorCo/3D-G, and 20 wt.% Pt/C; (b) Tafel; (c) the number of electrons transferred and H_2O_2 yields got from RRDE; (d) the poisoning experiments for M-PImPorCo/3D-G (O_2-saturated 0.1 M KOH) with and without 0.05 M KSCN; (e) *i*–*t* curves; and (f) the ADT curves. The OER test of M-PImPorCo/3D-G, TNO_2PorCo/3D-G, RuO_2, and 3D-G in 1 mol·L^{-1} KOH: (g) LSV curves of M-PImPorCo/3D-G, N-PImPorCo/3D-G, and M-N-PImPorCo/3D-G, TmPorCo/3D-G, and 20 wt.% Pt/C; (h) Tafel; (i) the ADT curves; (j) ΔE calculation of ORR and OER; (k) comparison of $E_{1/2}$, electron transfer number, $E_{j=10}$, ΔE, Tafel (ORR), and Tafel (OER) for M-PImPorCo/3D-G and the other catalysts.

3.4 Oxygen evolution reaction performance evaluation

Enhanced OER activity was also obtained on M-PImPorCo/3D-G. As shown in Fig. 3(g), the OER LSV curves of the prepared catalysts were measured in a N_2 saturated 1 M KOH aqueous solution. The potentials at the current density of 10 mA·cm^{-2} for M-PImPorCo/3D-G, M-N-PImPorCo/3D-G, N-PImPorCo/3D-G, TmPorCo/3D-G, and RuO_2 catalyst are 1.49, 1.50, 1.51, 1.54, and 1.50 V vs. RHE, respectively, which proves that electron –CH_2–OH donor group can improve the catalytic performance of OER. The potential values at the current density 10 mA·cm^{-2} of TNO_2PorCo/3D-G, M-PImPorCo, 3D-G, and RuO_2 catalyst are 1.53, 1.52, 1.82, and 1.50 V vs. RHE, respectively (Fig. S22(a) in the ESM), which demonstrates that the anchoring of M-PImPorCo onto 3D-G enhances its catalytic OER performance. M-PImPorCo/3D-G outperforms TNO_2PorCo/3D-G and TmPorCo/3D-G, highlighting the positive impact of conjugation on OER catalysis. M-PImPorCo/3D-G exhibits an over potential of 260 mV at the current density of 10 mA·cm^{-2}, much lower than that of M-N-PImPorCo/3D-G (270 mV), N-PImPorCo/3D-G (280 mV), TNO_2PorCo/3D-G (300 mV), M-PImPorCo (290 mV), and TmPorCo/3D-G (295 mV), and even close to that of the commercial RuO_2 catalyst (268 mV), indicating that the electron donor groups and the conjugation structure could enhance the OER performance. Meanwhile, Tafel plots were also calculated to

reveal the activity of OER, the Tafel slopes are about 81.1, 143.2, 173.2, 151.1, and 64.7 mV·dec^{-1} for M-PImPorCo/3D-G, M-N-PImPorCo/3D-G, N-PImPorCo/3D-G, TmPorCo/3D-G, TNO_2PorCo/3D-G, and RuO_2, respectively, and Tafel slope of M-PImPorCo/3D-G is also close to that of RuO_2 (64.7 mV·dec^{-1}) in Fig. 3(h) and Fig. S22(b) in the ESM, implying favorable OER reaction kinetics. Moreover, after 5000 CV cycles (as part of the ADT), M-PImPorCo/3D-G exhibits an overpotential increased by 8 mV, which is lower than that of RuO_2 (30 mV) (Fig. 3(i)), and TNO_2PorCo/3D-G (18 mV) (Fig. S23 in the ESM). In the chronoamperometry curves (Fig. S24 in the ESM), M-PImPorCo/3D-G experiences only a current decrease of 7.5%, while TNO_2PorCo/3D-G, 3D-G, and RuO_2 demonstrate a decrease at approximately 9.7%, 22.6%, and 17.4%, respectively. The catalytic oxygen reaction bifunction performance (Fig. 3(j)) represented by potential difference (ΔE) = $E_{j=10} - E_{1/2}$ (where $E_{j=10}$ represents potential at a current density of 10 mA·cm^{-2}) reveals that M-PImPorCo/3D-G possesses a ΔE value of 0.58 V, which is better than Pt/C or RuO_2 (ΔE = 0.98 V). Figures S25 and S26 in the ESM show the double-layer capacitance (C_{dl}), the slope of M-PImPorCo/3D-G is 28.1 mF·cm^{-2}, which is higher than that of TNO_2PorCo/3D-G, confirming its larger electrochemical specific surface area (ECSA) relative to TNO_2PorCo/3D-G. Therefore, M-PImPorCo/3D-G has a fast catalytic oxygen kinetic process, the highest half-wave potential, the lowest potential ($E_{j=10}$), and the most efficient bifunctional catalytic oxygen performance (ΔE) (Fig. 3(k)) [15, 60–63].

3.5 Composition, morphology, structure, and valence state characterization after durability test

M-PImPorCo/3D-G after 5000 cycles CV (M-PImPorCo/3D-G-5000) was analyzed to verify the chemical stability of M-PImPorCo/3D-G. Figure 4(a) depicts the SEM image of M-PImPorCo/3D-G-5000, revealing that its porous configuration remains intact and is not compromised during the electrocatalytic reaction. Figures 4(b) and 4(c) present the TEM and HRTEM images of M-PImPorCo/3D-G-5000, respectively. After undergoing electrocatalytic testing, M-PImPorCo retains foam-like graphene structure. In the HRTEM image, no lattice of atomic clusters or metal oxidation was observed in M-PImPorCo/3D-G, and it remains an amorphous structure. The staggered distribution of elements in HAADF-STEM (Fig. 4(d)) and uniform distribution of elements in mapping (Figs. 4(e)–4(g)) could be observed. Figure 4(h) exhibits the XRD pattern of M-PImPorCo/3D-G-5000, which still manifested as an amorphous diffuse reflection. Figure 4(i) presents full XPS spectrum of M-PImPorCo/3D-G-5000, indicating that all elements remained stably present. To further analyze the valence states of each element, the convolution peaks of C 1s (Fig. 4(j)), N 1s (Fig. 4(k)), and Co 2p (Fig. 4(l)) were examined (Table S2 in the ESM). Each element still maintains the structure before oxygen catalytic reaction, and the existence state and valence state of each element have not changed. These results align with the structural characterization before and after the CV tests, indicating that M-PImPorCo retains its structural integrity

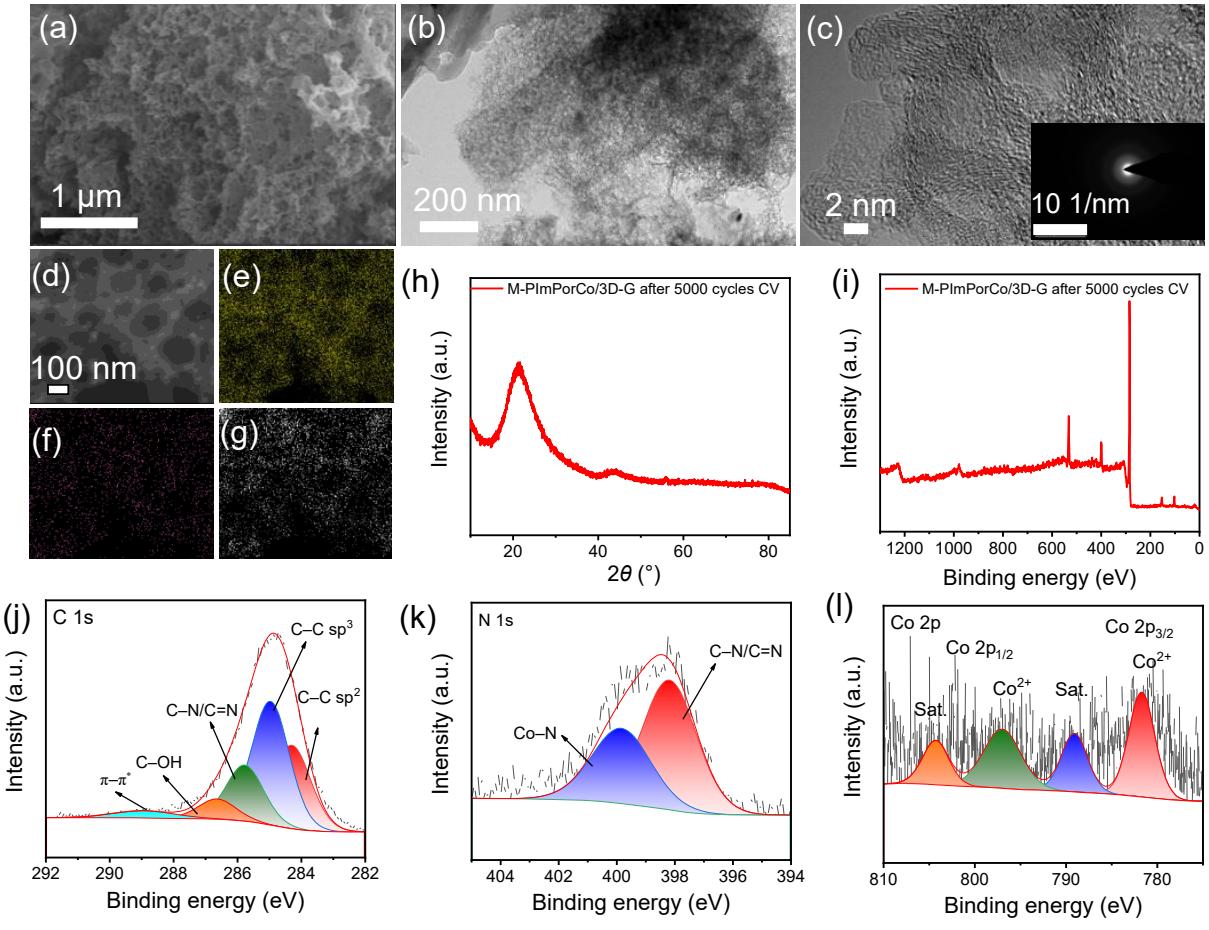

Figure 4 The characterization after durability test: (a) SEM image of M-PImPorCo/3D-G-5000; ((b) and (c)) TEM and HRTEM images of M-PImPorCo/3D-G-5000; (d) HAADF-STEM image; ((e)–(g)) mappings of overlayer, C, N, and Co; (h) XRD pattern of M-PImPorCo/3D-G-5000; (i) XPS full spectrum; ((j)–(l)) the high-resolution XPS spectra of M-PImPorCo/3D-G-5000: (j) C 1s, (k) N 1s, and (l) Co 2p.

during durability test. The absence of decomposition, aggregation, or stacking suggests that M-PImPorCo remains nearly monolayered on the 3D-G surface.

3.6 DFT calculations

To further explore the internal catalytic mechanism of M-PImPorCo/3D-G, DFT was introduced to calculate its structure and oxygen catalytic process. According to its own structure, Materials Studio 2019 was used to build a repetitive unit model for it, and DMol^3 module was used to calculate HOMO–LUMO energy before and after polymerization reaction. Based on the energy step diagram shown in Fig. 5(a), M-PImPorCo is only 1.569 eV, which is smaller than the energy of TNO_2PorCo. The decrease of HOMO–LUMO energy indicates that M-PImPorCo has a stronger electron gain and loss energy than monocyclic porphyrin [64], which is conducive to electron transfer in the catalytic reaction. Figures 5(b) and 5(c) show the electrostatic potential (ESP) of monocyclic porphyrin (Fig. 5(b)) and M-PImPorCo (Fig. 5(c)) repeating units, where red and blue represent large and small electron cloud density, respectively, and Co–N_4 in M-PImPorCo has a larger electron cloud density compared with monocyclic porphyrin. Therefore, the C=N group can attract the electron cloud density on the edge CH_2–OH to the Co–N_4 site, thereby improving its oxygen catalytic performance.

Models for TNO_2PorCo/3D-G and M-PImPorCo/3D-G (Fig. 5(d)) were built, and the structural optimization was carried out using Cambridge Serial Total Energy Package (CASTEP) module. According to the 4e$^-$ process involved in oxygen catalysis, the adsorption intermediate state was constructed, and ORR processed at electrode potential (U) = 0 V and OER processed at U = 1.23 V were calculated by using Vienna *ab initio* simulation package (VASP) software and first principles. Figures 5(e) and 5(f) show the adsorption step diagram, which clearly shows that the protonation process (OOH*, OH*) of ORR process requires lower Gibbs energy compared to mono-ring porphyrins. This proves that M-PImPorCo in nitrogen-rich environment is more favorable to protonation during oxygen catalysis. Density of states (DOS) calculates the d-band center of M-PImPorCo and TNO_2PorCo, and the d-band center of M-PImPorCo is further away from the Fermi level than TNO_2PorCo (Fig. 5(g)). Downward shift of the d-band center indicates that there is a smaller energy level in the intermediate desorption process, and M-PImPorCo has a fast kinetic process [44]. At the same time, the downward shift in the center of the d-band also implies that the active sites of M-PImPorCo have a richer electron cloud density. CASTEP module was employed to simulate internal electron transfer processes in TNO_2PorCo/3D-G and M-PImPorCo/3D-G. Figures 5(h) and 5(i) show the existence of electron transfer between TNO_2PorCo and

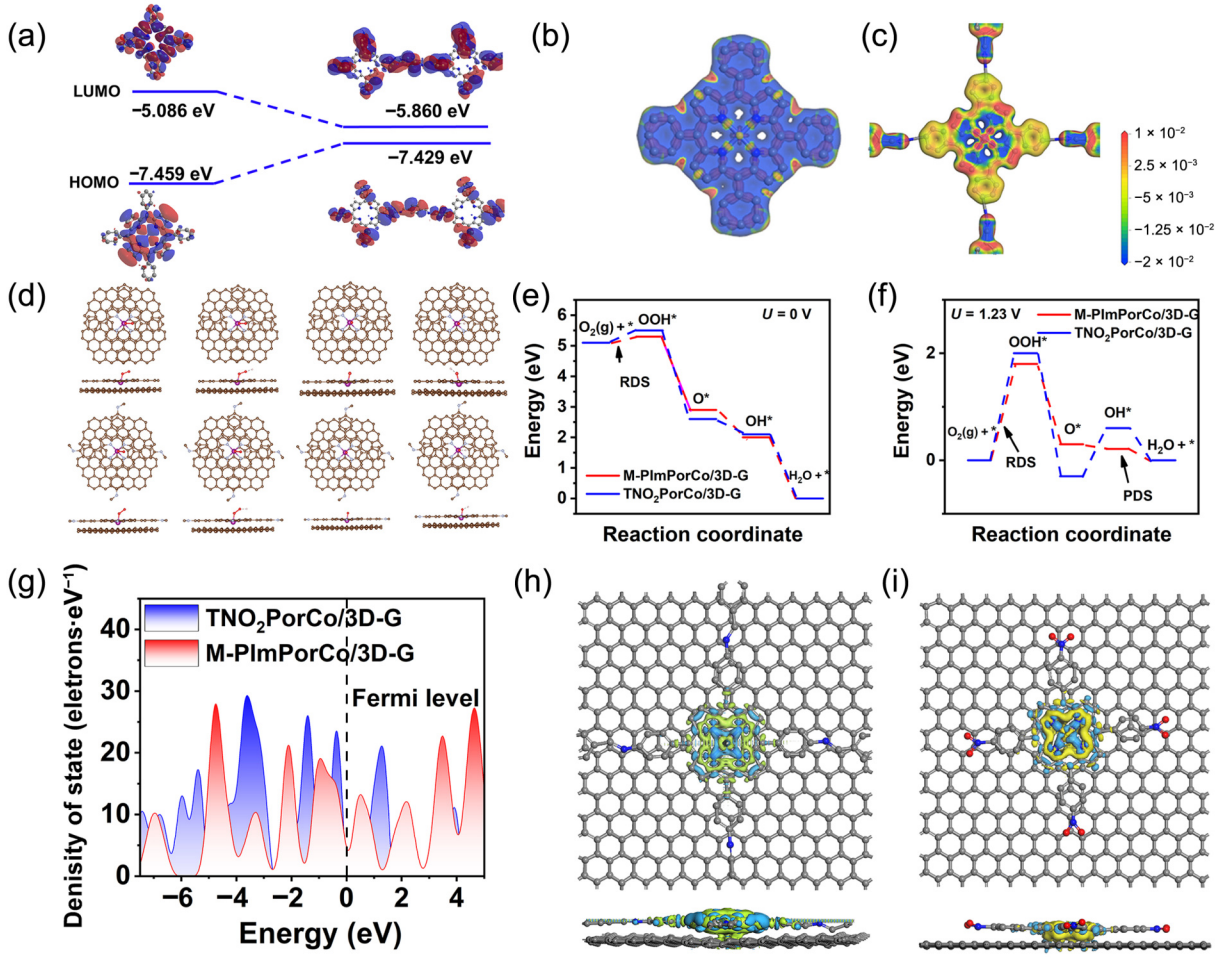

Figure 5 DFT calculation: (a) the energy levels of the HOMO and LUMO of TNO_2PorCo and M-PImPorCo; ((b) and (c)) the ESP; (d) M-PImPorCo/3D-G and TNO_2PorCo/3D-G repeating unit (Co–N_4 site); ((e) and (f)) Gibbs free energy change (ΔG) of TNO_2PorCo and M-PImPorCo after ORR and OER; (g) DOS of TNO_2PorCo and M-PImPorCo; ((h) and (i)) electron density difference analysis images of TNO_2PorCo/3D-G and M-PImPorCo/3D-G.

3D-G, which is mainly due to the π–π interaction formed by the π bond of porphyrin with 3D-G. The stronger electron transfer between M-PImPorCo and 3D-G is because: (1) M-PImPorCo has a larger conjugated system and a larger π bond, and (2) C=N is an electron-withdrawing group that can transfer electrons from 3D-G to Co–N_4 more quickly. It can be clearly seen that the Co–N_4 sites of M-PImPorCo/3D-G have a richer electron cloud density. Based on the above results, the reasons for the high oxygen catalytic performance of M-PImPorCo are as follows: (1) The fully conjugated COF has a smaller HOMO–LUMO energy, which makes COF quickly gain and lose electron in catalytic oxygen reaction; (2) nitrogen-rich COF is more favorable to the protonation process of oxygen catalysis; (3) the larger π bond of M-PImPorCo enhances the π–π interaction with 3D-G; (4) C=N, as a strong electron absorbing group, can attract the electron cloud density on the 3D-G surface and increase the electron cloud density at the Co–N_4 site; and (5) similarly, the edge groups of electron-rich CH_2–OH are attracted by C=N and transferred to the Co–N_4 site, forming an "electron donor–electron pump–electron acceptor" synergetic relationship to enhance the bifunction oxygen performance of M-PImPorCo/3D-G.

3.7 Liquid Zn-air batteries evaluation

To further assess the practical feasibility of the catalysts for bifunctional oxygen catalytic applications, liquid ZABs were assembled by using M-PImPorCo/3D-G supported by carbon cloth as the air cathode (Fig. 6(a)). As shown in Fig. S27 in the ESM, liquid M-PImPorCo/3D-G-based ZAB shows an open-circuit voltage (OCV) of 1.48 V, outperforming that of the liquid Pt/C+RuO_2-based ZAB (1.38 V). From Fig. 6(b), liquid M-PImPorCo/3D-G-based ZAB demonstrates maximum power density of 287.8 mW·cm^{-2}, higher than that of the Pt/C+RuO_2-based ZAB (170.1 mW·cm^{-2}). The polarization curves, shown in Fig. 6(c), provide insights into the performance of ZABs during discharge and charge processes. M-PImPorCo/3D-G-based ZAB exhibits a smaller voltage gap (0.65 V) than that of Pt/C+RuO_2-based ZAB (1.30 V) at the current density of 50 mA·cm^{-2}, indicating a better charge and discharge capacity. Furthermore, the discharge curves of M-PImPorCo/3D-G-based ZAB at different current densities of 10 mA·cm^{-2} are shown in Fig. 6(d), in which the specific capacity normalized to the loss mass of zinc plate is as large as 801.2 mAh·g_{Zn}^{-1} at 10 mA·cm^{-2}, higher than that of Pt/C+RuO_2-based ZAB (620.1 mAh·g_{Zn}^{-1}) and TNO_2PorCo-based ZAB (650.6 mAh·g_{Zn}^{-1}). Specific capacity of M-PImPorCo/3D-G-based ZAB is superior to most of single atom catalysts-based ZABs reported by previous Ref. [65]. Figure 6(e) shows the electrochemical impedance spectra (EIS) of several ZABs, with Ohmic resistance (R_Ω) representing the impedance of the materials and electrolytes in the ZABs and charge-transfer resistance (R_{ct}) representing the interfacial transfer resistance. Arc radius is the sum of the internal resistance and the interfacial transfer resistance. R_Ω of ZAB containing M-PImPorCo/3D-G is 1.23 Ω, and R_{ct} is 7.06 Ω. Both R_Ω and R_{ct} are smaller than those of ZAB containing TNO_2PorCo (R_Ω = 1.60 Ω and R_{ct} = 14.30 Ω) and ZAB assembled with Pt/C+RuO_2 (R_Ω = 1.26 Ω and R_{ct} = 17.0 Ω). Diffusion process in the Nyquist plot of M-PImPorCo/3D-G is closest to 45°, which proves that it has the fastest charge transfer process and mass transfer process.

Figure S28 in the ESM shows that the discharge voltage of M-PImPorCo/3D-G-based ZAB remains almost unchanged compared with the initial voltage, after discharging measurements at a series of different current densities from 10 to 80 mA·cm^{-2}, implying the superior stability of the M-PImPorCo/3D-G. As an example of the application of M-PImPorCo/3D-G-based ZAB, a red light-emitting diode (LED) light of the "SDUT" logo is lit by two liquid M-PImPorCo/3D-G-based ZABs (Fig. S29 in the ESM). To further evaluate the recharge ability of M-PImPorCo/3D-G ZAB, cycling stability was tested for 230 h by the charge–discharge measurement at 10 mA·cm^{-2}. There is no obvious change in the charge–discharge potential gap as observed in Fig. 6(f). In contrast, Pt/C+RuO_2-based ZAB exhibits slightly poor stability, which dramatically increases the charge–discharge potential gap after 20 h. This suggests that M-PImPorCo/3D-G exhibits excellent recharge ability and long-term cyclic stability. The above data further confirms that ZABs could provide a stable and reliable power source for practical applications, and the power density and discharge/charge cycling time surpass most of catalysts-based ZABs reported by previous literature (Table S4 in the ESM) [66–70].

3.8 Flexible Zn-air batteries evaluation

To improve the safety and portability of ZABs, all solid-state zinc-air batteries were also constructed using M-PImPorCo/3D-G as the catalyst for the air cathode. As displayed in Fig. 6(g), the schematic graph of all solid-state ZAB setup is presented. M-PImPorCo/3D-G is supported by carbon cloth combined with nickel foam as the cathode, which was assembled with polyvinyl alcohol (PVA) electrolyte and anodic zinc plate. OCV curves of all-solid ZAB with M-PImPorCo/3D-G are measured to be 1.51 V, which is higher than that of all-solid ZAB with Pt/C+RuO_2, as depicted in Fig. S30 in the ESM. From Fig. 6(h), all-solid ZAB with M-PImPorCo/3D-G displays the power density of 95.4 mW·cm^{-2}, superior to that of all-solid ZAB with Pt/C+RuO_2 (44.3 mW·cm^{-2}). Polarization curves of all-solid ZAB with M-PImPorCo/3D-G exhibit a voltage gap (0.70 V) at the current density of 20 mA·cm^{-2} (Fig. S31 in the ESM), implying a higher charge and discharge capacity. A red LED of the "SDUT" logo (Fig. S32 in the ESM) was also powered up by two solid state ZABs with M-PImPorCo/3D-G, implying the potential commercial application of M-PImPorCo/3D-G. As depicted in Fig. 6(i), the charge–discharge cycle stability of M-PImPorCo/3D-G is better than that of Pt/C+RuO_2 after 22.3 h. Under the constant current of 10 mA·cm^{-2}, M-PImPorCo/3D-G-ZABs can discharge stably for 20 h, which is more stable than Pt/C+RuO_2 (10.2 h) and TNO_2PorCo/3D-G (16.5 h) (Fig. 6(j)). Discharge and charge curves were also measured under bending conditions to evaluate the stability and flexibility of the ZABs (Fig. 6(k)). There is no significant change in the potential gap compared to the flat conditions, which indicates that the bending of the ZABs does not have a pronounced impact on the overall electrochemical behavior and performance of the battery.

4 Conclusions

In conclusion, the redox reaction of TNO_2PorCo and 1,4-phenyldimethyl alcohol was catalyzed by $RuCl_3$ to prepare different group modified fully conjugated poly (1,4-phenyldiimide phenylporphyrin) cobalt. Methylene alcohol terminated COF (M-PImPorCo) is a fully conjugated COF with electron-donating edge group modification. Topology simulation and PXRD of M-PImPorCo show that M-PImPorCo is mainly A–A stack type. Combined with TG, M-PImPorCo does not decompose at 600 °C.

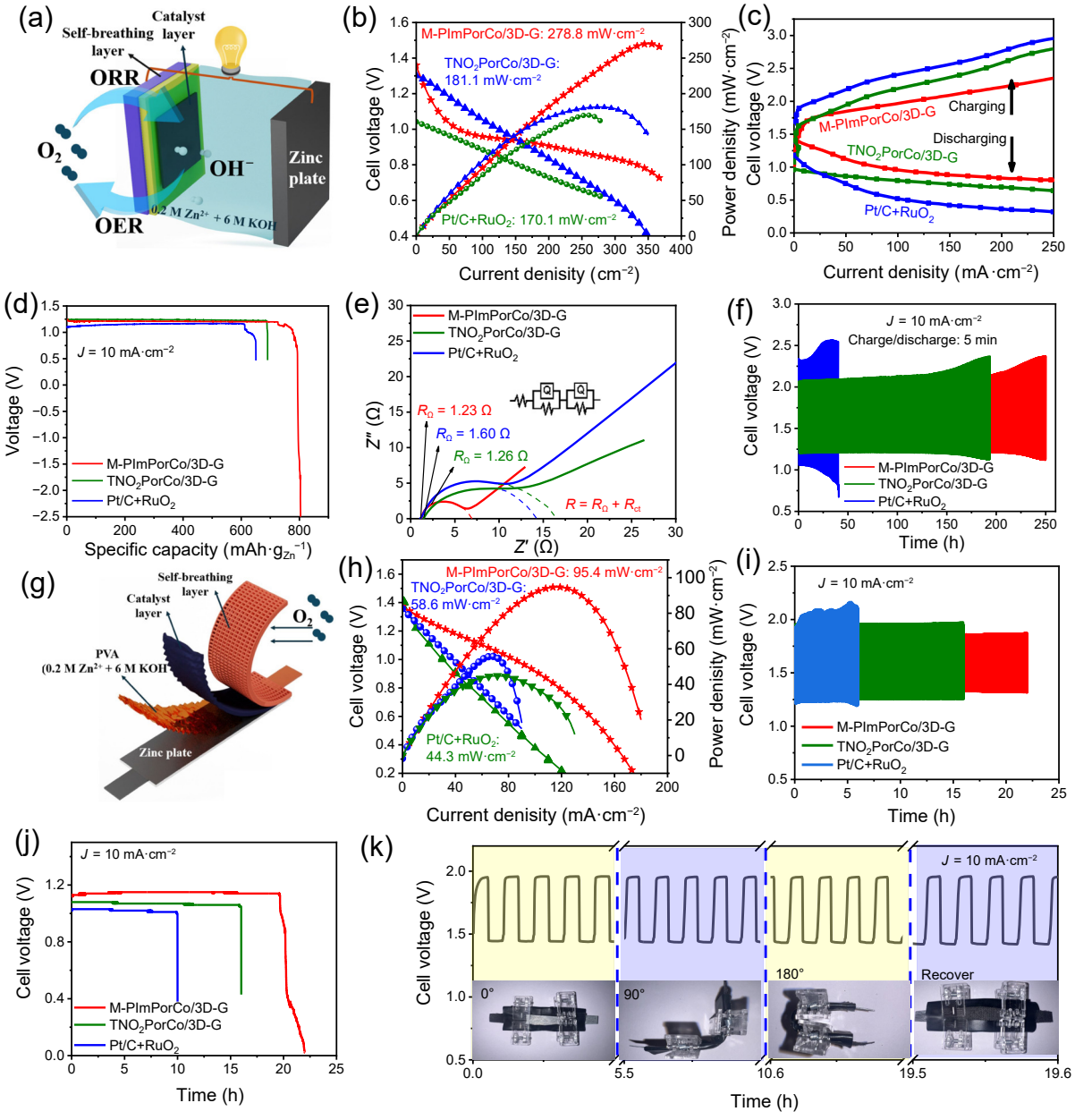

Figure 6 The Zn-air batteries performance evaluation: (a) model diagram of Zn-air battery; (b) the discharge curves of ZABs; (c) the charge and discharge polarization curves of Zn-air battery; (d) specific capacity of ZABs (~ 10 mA·cm^{-2}); (e) EIS test of ZABs; (f) the cyclic stability performance curves of ZAB at 10 mA·cm^{-2}; (g) schematic diagram of F-ZABs; (h) the power density of F-ZABs; (i) cycling stability of the solid flexible Zn-air battery; (j) specific capacity of ZABs (~ 10 mA·cm^{-2}); (k) galvanostatic discharge and charge curves of Zn-air battery with the M-PImPorCo/3D-G cathodes under bending.

Compared with monocyclic porphyrins, M-PImPorCo has a lower HOMO–LUMO energy gap, indicating that it is easier to gain and lose electrons in catalytic reactions. C=N group and –CH_2–OH edge group can act as an "electron pump" to enhance the electron cloud density of Co–N_4. M-PImPorCo is anchored on the 3D-G surface by enhanced impregnation. The PXRD, Raman, and XPS analyses of M-PImPorCo/3D-G show that M-PImPorCo is not decomposed after HT and is laid on the 3D-G surface. π–π interaction between M-PImPorCo and 3D-G improves the electron cloud density of Co–N_4 site in M-PImPorCo, thereby increasing the catalytic oxygen reaction activity. M-PImPorCo/3D-G showed significant catalytic oxygen reaction bifunctional performance (0.58 V) with $E_{1/2}$ = 0.91 V vs. RHE and $E_{j=10}$ = 1.49 V vs. RHE. The activity order of samples is M-PImPorCo/3D-G > M-N-PImPorCo/3D-G > N-PImPorCo/3D-G > TmPorCo/3D-G > TNO_2PorCo/3D-G. These results show that electron donor groups and the effect of conjugation can improve the catalytic activity. Both ZABs and flexible ZABs (F-ZABs) equipped with M-PImPorCo/3D-G showed excellent charge–discharge performance, which also demonstrated good bifunctional oxygen catalytic activity. This work provides a facile method for the synthesis strategy of fully conjugated Schiff base metal porphyrin COF, and provides an efficient bifunctional oxygen catalyst for energy storage device.

Electronic Supplementary Material: Supplementary material (experimental details, materials characterizations, and additional figures and tables) is available in the online version of this article at https://doi.org/10.26599/NR.2025.94907789.

Data availability

All data needed to support the conclusions in the paper are presented in the manuscript and the Electronic Supplementary Material. Additional data related to this paper may be requested from the corresponding author upon request.

Acknowledgements

This work was financially supported by the National Natural Science Foundation of China (Nos. 22172093 and 21776167) and the Natural Science Foundation of Shandong Province, China (No. ZR2023MB061).

Declaration of competing interest

All the contributing authors report no conflict of interests in this work.

Author contribution statement

Y. G. S.: Investigation, writing – original draft, formal analysis, software. P. S.: Resources, methodology, writing – review & editing. J. G. W.: Writing – review & editing, resources, methodology. Y. Q. Z.: Resources, methodology. L. K. W.: Resources, methodology. A. L.: Resources, methodology. Z. F. L.: Conceptualization, supervision, validation, writing – review & editing, funding acquisition. All the authors have approved the final manuscript.

Use of AI statement

None.

References

[1] Dou, Y. Q.; Wang, A. J.; Zhao, L.; Yang, X.; Wang, Q.; Shire Sudi, M.; Zhu, W. H.; Shang, D. H. Boosted hydrogen evolution reaction for a nitrogen-rich azo-bridged metallated porphyrin network. *J. Colloid Interface Sci.* **2023**, *650*, 943–950.

[2] Zhang, Q. N.; Dong, S. D.; Shao, P. P.; Zhu, Y. H.; Mu, Z. J.; Sheng, D. F.; Zhang, T.; Jiang, X.; Shao, R. W.; Ren, Z. X. Covalent organic framework-based porous ionomers for high-performance fuel cells. *Science* **2022**, *378*, 181–186.

[3] Jiang, Y. Y.; Li, P. F.; Li, Z.; Zhang, B. B.; Li, S. Y. Photoenzymatic synthesis of 1-alkenes and hydroxyl fatty acids by cascading a COF photocatalyst and P450 peroxygenases. *Sci. Bull.* **2024**, *69*, 3350–3354.

[4] Armillotta, F.; Bidoggia, D.; Baronio, S.; Biasin, P.; Annese, A.; Scardamaglia, M.; Zhu, S. Y.; Bozzini, B.; Modesti, S.; Peressi, M. et al. Single metal atom catalysts and ORR: H-bonding, solvation, and the elusive hydroperoxyl intermediate. *ACS Catal.* **2022**, *12*, 7950–7959.

[5] Li, Q. Q.; Sun, C.; Sun, X. L.; Yin, Z. J.; Du, Y. P.; Liu, J. C.; Luo, F. Synthesis of palladium-rare earth alloy as a high-performance bifunctional catalyst for direct ethanol fuel cells. *Nano Res.* **2024**, *17*, 9525–9531.

[6] Huang, S. D.; Zhang, B. Y.; Wu, D. S.; Xu, Y. F.; Hu, H. Y.; Duan, F.; Zhu, H.; Du, M. L.; Lu, S. L. Linkage engineering in covalent organic frameworks as metal-free oxygen reduction electrocatalysts for hydrogen peroxide production. *Appl. Catal. B: Environ.* **2024**, *340*, 123216.

[7] Liu, Y. P.; Bao, J. H.; Li, Z. F.; Zhang, L.; Zhang, S. Z.; Wang, L. K.; Niu, X. L.; Sun, P.; Xu, L. P. Large-scale defect-rich iron/nitrogen co-doped graphene-based materials as the excellent bifunctional electrocatalyst for liquid and flexible all-solid-state zinc-air batteries. *J. Colloid Interface Sci.* **2022**, *607*, 1201–1214.

[8] Wang, M. H.; Dong, Q.; Ji, S.; Wang, H.; Peng, J.; Wang, X. Y.; Linkov, V.; Teng, C.; Wang, R. F. "Coupling-conversion" effect induced by interface-local electric field to improve oxygen reaction kinetics in zinc-air batteries. *Chem. Eng. J.* **2024**, *481*, 148601.

[9] Qin, H. N.; Kong, J. F.; Peng, X. Y.; Wang, Z. M.; Li, X. L.; Lei, H. T.; Zhang, W.; Cao, R. Revealing significant electronic effects on the oxygen reduction reaction with iron porphyrins. *ChemSusChem* **2024**, *18*, e202401739.

[10] Li, X. L.; Zhang, X. P.; Guo, M.; Lv, B.; Guo, K.; Jin, X. T.; Zhang, W.; Lee, Y. M.; Fukuzumi, S.; Nam, W. et al. Identifying intermediates in electrocatalytic water oxidation with a manganese corrole complex. *J. Am. Chem. Soc.* **2021**, *143*, 14613–14621.

[11] Liu, T.; Meng, J.; Qin, H. N.; Zhang, M. C.; Sun, N.; Mei, B. X.; Li, H. M.; Zhang, X. P.; Li, J.; Cao, R. Mechanistic studies of catalytic O_2-to-H_2O_2 conversion at a single cobalt site. *J. Am. Chem. Soc.* **2025**, *147*, 22322–22328.

[12] Mu, C.; Wang, B.; Yao, Q. F.; He, Q.; Xie, J. P. Composition-dependent catalytic performance of Au_xAg_{25-x} alloy nanoclusters for oxygen reduction reaction. *Nano Res.* **2024**, *17*, 9490–9497.

[13] Li, Z. W.; Shi, X. R.; Cheng, H. J.; Song, Y. R.; Jiao, Y. Y.; Shi, S. B.; Gao, J. F.; Hou, J. G. Atomically dispersed iron active sites on covalent organic frameworks for artificial photosynthesis of hydrogen peroxide. *Adv. Energy Mater.* **2024**, *14*, 2302797.

[14] Liu, M. M.; Zhu, X. H.; Song, Y. J.; Huang, G. L.; Wei, J. M.; Song, X. K.; Xiao, Q.; Zhao, T.; Jiang, W.; Li, X. P. et al. Bifunctional edge-rich nitrogen doped porous carbon for activating oxygen and sulfur. *Adv. Funct. Mater.* **2023**, *33*, 2213395.

[15] Liu, M. H.; Liu, S. J.; Cui, C. X.; Miao, Q. Y.; He, Y.; Li, X. W.; Xu, Q.; Zeng, G. F. Construction of catalytic covalent organic frameworks with redox-active sites for the oxygen reduction and the oxygen evolution reaction. *Angew. Chem., Int. Ed.* **2022**, *61*, e202213522.

[16] Yan, X. Y.; Wang, B. B.; Ren, J.; Long, X. J.; Yang, D. J. An unsaturated bond strategy to regulate active centers of metal-free covalent organic frameworks for efficient oxygen reduction. *Angew. Chem., Int. Ed.* **2022**, *61*, e202209583.

[17] Sun, Y. G.; Sun, P.; Wang, J. G.; Zhuang, Y. Q.; Wu, Y. N.; Li, Z. F. Mn–N_5 structure between poly-porphyrin manganese and 3D N-doped graphene to enhance bifunctional oxygen catalytic performance. *J. Colloid Interface Sci.* **2025**, *686*, 711–721.

[18] Sun, Y. G.; Duan, W. J.; Wang, J. G.; Sun, P.; Zhuang, Y. Q.; Li, Z. F. A novel fully conjugated COF adorned on 3D-G to boost the "D–π–A" electron regulation in oxygen catalysis performance. *Chem. Sci.* **2025**, *16*, 9951–9965.

[19] Zhang, D. H.; Si, L. X.; Ren, Q. Q.; Yan, X. T.; Hu, S. Competitive intermetallics formation in Pd–Zn–Cd system via seeded growth from ultra-thin Pd nanosheets for electrocatalytic ethanol oxidation reaction. *Nano Res.* **2024**, *17*, 8552–8559.

[20] Sun, Y. G.; Zhang, T. W.; Sun, P.; Wang, J. G.; Duan, W. J.; Zhuang, Y. Q.; Wang, L. K.; Li, Z. F. Enhanced bifunctional oxygen electrochemical catalytic performance using La-doped $CoFe_2O_4$ spinel supported by 3D-G for Zn-air batteries. *J. Energy Chem.* **2024**, *94*, 778–788.

[21] Feng, Z. Q.; Honda, S.; Ohyama, J.; Iwata, Y.; Awaya, K.; Yoshida, H.; Machida, M.; Higashi, K.; Uruga, T.; Kawamura, N. et al. Structural effects of FeN_4 active sites surrounded by fourteen-membered ring ligands on oxygen reduction reaction activity and durability. *ACS Catal.* **2024**, *14*, 7416–7425.

[22] Wang, C.; Liu, Y. P.; Li, Z. F.; Wang, L. K.; Niu, X. L.; Sun, P. Novel space-confinement synthesis of two-dimensional Fe, N-codoped graphene bifunctional oxygen electrocatalyst for rechargeable air-cathode. *Chem. Eng. J.* **2021**, *411*, 128492.

[23] Yang, X. X.; Zhao, S.; Zhang, Z. Z.; Chi, Y.; Yang, C. M.; Wang, C. T.; Zhen, Y. Z.; Wang, D. J.; Fu, F.; Chi, R. A. Pore structure regulation of hierarchical porous carbon derived from coal tar pitch via pre-oxidation strategy for high-performance supercapacitor. *J. Colloid Interface Sci.* **2022**, *614*, 298–309.

[24] Zhou, Y. N.; Sheng, L.; Chen, L. L.; Zhao, W. H.; Zhang, W. H.; Yang, J. L. Metal and ligand modification modulates the electrocatalytic HER, OER, and ORR activity of 2D conductive metal–organic frameworks. *Nano Res.* **2024**, *17*, 7984–7990.
[25] Deng, C.; Wang, T.; Wu, P. W.; Zhu, W. S.; Dai, S. High entropy materials for catalysis: A critical review of fundamental concepts and applications. *Nano Energy* **2024**, *120*, 109153.
[26] Zou, Y. N.; Su, Y. Y.; Yu, Y. C.; Luo, J. L.; Kang, X. M.; Zhang, J.; Lan, L. H.; Wang, T. S.; Li, J. On the role of Zn and Fe doping in nitrogen-carbon electrocatalysts for oxygen reduction. *Nano Res.* **2024**, *17*, 9564–9572.
[27] Greeley, J.; Stephens, I. E. L.; Bondarenko, A. S.; Johansson, T. P.; Hansen, H. A.; Jaramillo, T. F.; Rossmeisl, J.; Chorkendorff, I.; Nørskov, J. K. Alloys of platinum and early transition metals as oxygen reduction electrocatalysts. *Nat. Chem.* **2009**, *1*, 552–556.
[28] Zhao, Y. Y.; Yang, C. Y.; Zhang, S. M.; Sun, G. T.; Zhu, B. C.; Wang, L. X.; Zhang, J. J. Investigating the charge transfer mechanism of ZnSe QD/COF S-scheme photocatalyst for H_2O_2 production by using femtosecond transient absorption spectroscopy. *Chin. J. Catal.* **2024**, *63*, 258–269.
[29] Zhang, Z.; Wang, W. W.; Wang, X. N.; Zhang, L.; Cheng, C.; Liu, X. K. Ladder-type π-conjugated metallophthalocyanine covalent organic frameworks with boosted oxygen reduction reaction activity and durability for zinc-air batteries. *Chem. Eng. J.* **2022**, *435*, 133872.
[30] Luo, F.; Li, M.; Yang, Z. H. Ultrafine $CoFe_2O_4$ quantum dots as an oxygen electrocatalyst for rechargeable zinc air batteries. *Chem. Commun.* **2022**, *58*, 13739–13742.
[31] Liu, M.; Wang, Y. R.; Ding, H. M.; Lu, M.; Gao, G. K.; Dong, L. Z.; Li, Q.; Chen, Y. F.; Li, S. L.; Lan, Y. Q. Self-assembly of anthraquinone covalent organic frameworks as 1D superstructures for highly efficient CO_2 electroreduction to CH_4. *Sci. Bull.* **2021**, *66*, 1659–1668.
[32] Huang, Y.; Chen, Y. C.; Xu, M. J.; Ly, A.; Gili, A.; Murphy, E.; Asset, T.; Liu, Y. C.; De Andrade, V.; Segre, C. U. et al. Catalysts by pyrolysis: Transforming metal–organic frameworks (MOFs) precursors into metal-nitrogen-carbon (M-N-C) materials. *Mater. Today* **2023**, *69*, 66–78.
[33] Shen, M. X.; Liu, J.; Li, J.; Duan, C.; Xiong, C. Y.; Zhao, W.; Dai, L.; Wang, Q. Y.; Yang, H.; Ni, Y. H. Breaking the N-limitation with N-enriched porous submicron carbon spheres anchored Fe single-atom catalyst for superior oxygen reduction reaction and Zn-air batteries. *Energy Storage Mater.* **2023**, *59*, 102790.
[34] Liu, Y. P.; Li, Z. F.; Sun, C. Y.; Wang, S. F.; Wang, L. K.; Niu, X. L.; Sun, P.; Zhang, S. Z. Closely packed planar polyphthalocyanine iron/hierarchical three-dimensional graphene as an oxygen electrocatalyst for the ORR and OER, and zinc-air batteries. *Sustain. Energy Fuels* **2021**, *5*, 5216–5226.
[35] Peng, P.; Shi, L.; Huo, F.; Mi, C. X.; Wu, X. H.; Zhang, S. J.; Xiang, Z. H. A pyrolysis-free path toward superiorly catalytic nitrogen-coordinated single atom. *Sci. Adv.* **2019**, *5*, eaaw2322.
[36] Zhu, Y. W.; Gan, L.; Shi, J. Q.; Huang, G.; Gao, H. M.; Tao, L.; Wang, S. Y. Co–CoF_2 heterojunctions encapsulated in N, F co-doped porous carbon as bifunctional oxygen electrocatalysts for Zn-air batteries. *Chem. Eng. J.* **2022**, *433*, 133541.
[37] Li, Z. F.; Yang, J. W.; Xu, G. F.; Wang, S. W. Non-precious cathode electrocatalyst for magnesium air fuel cells: Activity and durability of iron-polyphthalocyanine absorbed on carbon black. *J. Power Sources* **2013**, *242*, 157–165.
[38] Xu, Z. L.; Duan, Q.; Cui, X. Copper-porphyrin-based covalent organic frameworks for efficient water remediation: A synergistic strategy of adsorption and photo-self-Fenton degradation. *Chem. Eng. J.* **2025**, *511*, 162241.
[39] Zhuang, Y. Q.; Sun, Y. G.; Wang, L. K.; Sun, P.; Wang, J. G.; Zhang, P. H.; Li, Z. F. Full conjugated poly(1,4-phenyldiazo porphyrin cobalt) covalent organic framework with D–π–A structure enhancing bifunctional oxygen catalytic performance. *J. Energy Chem.* **2025**, *104*, 214–224.
[40] Huang, Y. P.; Liu, K.; Kan, S. T.; Liu, P. G.; Hao, R.; Liu, W. F.; Wu, Y. F.; Liu, H. T.; Liu, M.; Liu, K. Y. Highly dispersed Fe–N_x active sites on graphitic-N dominated porous carbon for synergetic catalysis of oxygen reduction reaction. *Carbon* **2021**, *171*, 1–9.
[41] Yue, Y.; Cai, P. Y.; Xu, K.; Li, H. Y.; Chen, H. Z.; Zhou, H. C.; Huang, N. Stable bimetallic polyphthalocyanine covalent organic frameworks as superior electrocatalysts. *J. Am. Chem. Soc.* **2021**, *143*, 18052–18060.
[42] Ma, X. L.; Hu, J. Y.; Li, S. Z.; Zheng, T. Y.; Gao, Y.; Han, Y. S.; Pan, H. H.; Bian, Y. Z.; Jiang, J. Z. Porphyrin-based covalent organic frameworks with undulated layers for efficient photocatalytic CO_2 reduction. *Sci. Bull.*, in press, DOI: 10.1016/j.scib.2025.04.002.
[43] Wang, D. K.; Zeng, H.; Xiong, X.; Wu, M. F.; Xia, M. R.; Xie, M. L.; Zou, J. P.; Luo, S. L. Highly efficient charge transfer in CdS-covalent organic framework nanocomposites for stable photocatalytic hydrogen evolution under visible light. *Sci. Bull.* **2020**, *65*, 113–122.
[44] Jin, E. Q.; Asada, M.; Xu, Q.; Dalapati, S.; Addicoat, M. A.; Brady, M. A.; Xu, H.; Nakamura, T.; Heine, T.; Chen, Q. H. et al. Two-dimensional sp^2 carbon-conjugated covalent organic frameworks. *Science* **2017**, *357*, 673–676.
[45] Li, Z. E.; He, T.; Gong, Y. F.; Jiang, D. L. Covalent organic frameworks: Pore design and interface engineering. *Acc. Chem. Res.* **2020**, *53*, 1672–1685.
[46] Wang, S. F.; Li, Z. F.; Duan, W. J.; Sun, P.; Wang, J. G.; Liu, Q.; Zhang, L.; Zhuang, Y. Q. Conjugated polymerized bimetallic phthalocyanine based electrocatalyst with Fe–N_4/Co–N_4 dual-sites synergistic effect for zinc-air battery. *J. Energy Chem.* **2023**, *86*, 41–53.
[47] Lin, S.; Diercks, C. S.; Zhang, Y. B.; Kornienko, N.; Nichols, E. M.; Zhao, Y. B.; Paris, A. R.; Kim, D.; Yang, P. D.; Yaghi, O. M. et al. Covalent organic frameworks comprising cobalt porphyrins for catalytic CO_2 reduction in water. *Science* **2015**, *349*, 1208–1213.
[48] Lai, J. W.; Liu, S. K.; Ma, W. J.; Wu, F.; Yu, P.; Mao, L. Q. Steric effect of intermediates induces formation of three-dimensional covalent organic frameworks. *Nat. Commun.* **2025**, *16*, 6071.
[49] Feng, Y.; Wang, G.; Liu, R.; Ye, X.; Tao, S.; Addicoat, M. A.; Li, Z.; Jiang, Q.; Jiang, D. Photoresponsive covalent organic frameworks: Visible-light controlled conversion of porous structures and its impacts. *Angew. Chem., Int. Ed.* **2024**, *63*, e202400009.
[50] Zhong, Y. Q.; Zhang, Y. Z.; Wang, J. J.; Jin, H. L.; Pan, S.; Wang, S.; Chen, Y. H. Advancing extreme-temperature-tolerant zinc-air batteries through photothermal transition metal sulfide heterostructures. *Energy Environ. Sci.* **2025**, *18*, 991–1001.
[51] Sun, Y. G.; Du, X.; Wang, J. G.; Liu, Q.; Mu, J. L.; Li, Z. F.; Jiang, H. Q.; Wang, L. K. Interface engineering of Co nanoparticles decorated by Ir confined in N-doped carbon nanotubes for flexible Zn-air batteries and pH-universal overall water splitting. *Rare Met.* **2024**, *43*, 6447–6459.
[52] Zhi, Q. J.; Liu, W. P.; Jiang, R.; Zhan, X. N.; Jin, Y. C.; Chen, X.; Yang, X. Y.; Wang, K.; Cao, W.; Qi, D. D. et al. Piperazine-linked metalphthalocyanine frameworks for highly efficient visible-light-driven H_2O_2 photosynthesis. *J. Am. Chem. Soc.* **2022**, *144*, 21328–21336.
[53] Bao, R.; Xiang, Z. H.; Qiao, Z. L.; Yang, Y. P.; Zhang, Y. T.; Cao, D. P.; Wang, S. T. Designing thiophene-enriched fully conjugated 3D covalent organic framework as metal-free oxygen reduction catalyst for hydrogen fuel cells. *Angew. Chem., Int. Ed.* **2023**, *62*, e202216751.
[54] Zhang, X. C.; Cheng, S. L.; Chen, C.; Wen, X.; Miao, J.; Zhou, B. X.; Long, M. C.; Zhang, L. Z. Keto-anthraquinone covalent organic framework for H_2O_2 photosynthesis with oxygen and alkaline water. *Nat. Commun.* **2024**, *15*, 2649.
[55] Wei, J.; Zhao, C. C.; Chen, M.; Liu, F. Y.; Zhao, L. M.; Zhao, H.; Yuan, Z. Y. COF-derived Co nanoparticles@N-doped carbon electrocatalysts for high performance Zn-air batteries. *Chin. J. Chem. Eng.* **2023**, *63*, 43–50.
[56] Gong, C. T.; Peng, Y. W.; Xu, M. Q.; Wei, X. F.; Sheng, G.; Liu, J. L.; Wu, X. W.; Han, X.; Dai, F. N.; Dong, J. Q. et al. Selective

electrocatalytic synthesis of urea using entangled iron porphyrins in covalent organic frameworks. *Nat. Synth.* **2025**, *4*, 720–729.

[57] Hedau, B.; Ha, T. J. Indium-doped iron-coordinated covalent organic framework as an efficient bifunctional oxygen electrocatalyst for energy applications. *J. Alloy. Compd.* **2025**, *1010*, 178134.

[58] Bian, R. J.; Deng, Y.; Li, Y.; Li, P. F.; Gao, R. Y.; Luo, Y. L.; Lu, J. P.; Fan, C. H.; Liu, L. F.; Xia, Z. N. et al. Inducing exciton dissociation in covalent organic framework by local gradient ionic polarization for enhanced hydrogen peroxide photosynthesis. *Appl. Catal. B: Environ. Energy* **2025**, *371*, 125292.

[59] Cheng, F. Y.; Shen, J.; Peng, B.; Pan, Y. D.; Tao, Z. L.; Chen, J. Rapid room-temperature synthesis of nanocrystalline spinels as oxygen reduction and evolution electrocatalysts. *Nat. Chem.* **2011**, *3*, 79–84.

[60] Liu, S. H.; Wang, Z. Y.; Zhou, S.; Yu, F. J.; Yu, M. Z.; Chiang, C. Y.; Zhou, W. Z.; Zhao, J. J.; Qiu, J. S. Metal–organic-framework-derived hybrid carbon nanocages as a bifunctional electrocatalyst for oxygen reduction and evolution. *Adv. Mater.* **2017**, *29*, 1700874.

[61] Wang, J.; Li, W.; Li, Y.; Huang, A. Space-confined growth of Co_9S_8 nanoparticles in covalent organic framework-derived porous carbon for efficient bifunctional oxygen electrocatalysis. *Adv. Sustain. Syst.* **2024**, *8*, 2300301.

[62] Chen, Z. P.; Jiang, J. B.; Jing, M. J.; Bai, Y. S.; Zhang, X. Y.; Deng, W. H.; Wu, Y. F.; Chen, F.; Yi, M. G.; Yang, M. X. et al. Covalent organic framework-derived Fe, Co-nitrogen codoped carbon as a bifunctional electrocatalyst for rechargeable efficient Zn-air batteries. *Carbon Neutralizat.* **2024**, *3*, 689–699.

[63] Wu, X. L.; Han, G. S.; Wen, H.; Liu, Y. Y.; Han, L.; Cui, X. Y.; Kou, J. J.; Li, B. J.; Jiang, J. C. Co_2N nanoparticles anchored on N-doped active carbon as catalyst for oxygen reduction reaction in zinc-air battery. *Energy Environ. Mater.* **2022**, *5*, 935–943.

[64] Zhou, G. L.; Chen, K. Y.; Liang, G. M.; Long, J. L. Confined covalent organic framework anchored Fe sites derived highly uniform electrocatalysts for rechargeable aqueous and solid-state Zn-air batteries. *J. Colloid Interface Sci.* **2023**, *651*, 794–804.

[65] Feng, Y.; Song, K. X.; Zhang, W.; Zhou, X. Y.; Yoo, S. J.; Kim, J. G.; Qiao, S. F.; Qi, Y. G.; Zou, X.; Chen, Z. J. et al. Efficient ORR catalysts for zinc-air battery: Biomass-derived ultra-stable Co nanoparticles wrapped with graphitic layers via optimizing electron transfer. *J. Energy Chem.* **2022**, *70*, 211–218.

[66] Fan, H.; Yang, L. J.; Wang, Y.; Zhang, X. L.; Wu, Q. S.; Che, R. C.; Liu, M.; Wu, Q.; Wang, X. Z.; Hu, Z. Boosting oxygen reduction activity of spinel $CoFe_2O_4$ by strong interaction with hierarchical nitrogen-doped carbon nanocages. *Sci. Bull.* **2017**, *62*, 1365–1372.

[67] Alegre, C.; Busacca, C.; Di Blasi, A.; Cannilla, C.; Barbera, O.; Antonucci, V.; Lázaro, M. J.; Baglio, V. Electrospun $MnCo_2O_4$/carbon-nanofibers as oxygen electrode for alkaline zinc-air batteries. *J. Energy Storage* **2022**, *55*, 105404.

[68] Liu, X. M.; Cui, X. Y.; Dastafkan, K.; Wang, H. F.; Tang, C.; Zhao, C.; Chen, A. B.; He, C. X.; Han, M. H.; Zhang, Q. Recent advances in spinel-type electrocatalysts for bifunctional oxygen reduction and oxygen evolution reactions. *J. Energy Chem.* **2021**, *53*, 290–302.

[69] Zhang, Q.; Shen, T.; Song, M.; Wang, S.; Zhang, J. L.; Huang, X.; Lu, S. F.; Wang, D. L. High-entropy $L1_2$-$Pt(FeCoNiCuZn)_3$ intermetallics for ultrastable oxygen reduction reaction. *J. Energy Chem.* **2023**, *86*, 158–166.

[70] Zhao, Z. Q.; Hao, J. B.; Jia, B. N.; Zhang, X. H.; Wu, G.; Zhang, C. L.; Li, L.; Gao, S. L.; Ma, Y. R.; Li, Y. Z. et al. Transition metal embedded in nonmetal-doped T-carbon [110]: A superior synergistic trifunctional electrocatalyst for HER, OER and ORR. *J. Energy Chem.* **2023**, *83*, 79–89.